UCRL-51659

NUMERICAL STUDIES OF CRATERING IN BEARPAW SHALE: TWO-DIMENSIONAL RESULTS

Jon B. Bryan
Donald E. Burton
Marvin D. Denny

October 8, 1974

Prepared for U.S. Atomic Energy Commission under contract No. W-7405-Eng-48

LAWRENCE LIVERMORE LABORATORY
University of California/Livermore

Printed in the United States of America
Available from
National Technical Information Service
U.S. Department of Commerce
5285 Port Royal Road
Springfield, Virginia 22151
Price: Printed Copy $___*; Microfiche $1.45

*Pages	NTIS Selling Price
1-50	$4.00
51-150	$5.45
151-325	$7.60
326-500	$10.60
501-1000	$13.60

TID-4500, UC-35
Peaceful Applications
of Explosions

LAWRENCE LIVERMORE LABORATORY
University of California/Livermore, California/94550

UCRL-51659

NUMERICAL STUDIES OF CRATERING IN BEARPAW SHALE: TWO-DIMENSIONAL RESULTS

Jon B. Bryan
Donald E. Burton
Marvin D. Denny

MS. date: October 8, 1974

Foreword

This work was performed under the auspices of the Defense Nuclear Agency, the United States Atomic Energy Commission, and the Office of the Chief of Engineers and funded under Subtask Codes L19AAXSX301 and L19CAXSX302 (Crater Studies), Work Unit 02 (Theoretical Calculations).
Donald E. Burton was formerly with the U.S. Army Corps of Engineers Waterways Experiment Station Explosive Excavation Research Laboratory, Livermore, California.

Contents

NUMERICAL STUDIES OF CRATERING IN BEARPAW SHALE: TWO-DIMENSIONAL RESULTS

Abstract

The computer calculations described in this report were performed to simulate cratering phenomena associated with subsurface detonations in Bearpaw clay shale. These calculations and a complementary field program were part of Project Diamond Ore.

A cratering equivalence between nuclear and high explosives was established using the SOC and TENSOR stress-wave-propagation computer codes for dynamic modeling. Late-time ballistic and fallback modeling were utilized to define the final crater configurations. It was found necessary to run each calculation to at least 20 ms to get an accurate final representation.

Stemmed cratering calculations made at three burial depths (6, 12.5, and 17 m) and two source energies defined calculated nitromethane cratering curves which closely matched empirical curves. A hypothetical 20-ton nuclear source was analyzed in stemmed and unstemmed configurations. The cratering dynamics and final crater shapes were nearly the same for the 20-ton nuclear and 10-ton nitromethane stemmed sources, the crater dimensions and volumes differing by less than ±5%.

Introduction

The development and understanding of nuclear explosives as excavation tools requires testing in a variety of geologic media and near-surface emplacement configurations. Chemical explosives provide a convenient and economical way to model nuclear explosive effects. Computer simulation of cratering configurations can be used to establish a relationship (cratering equivalence) between high explosive and nuclear cratering sources. At the Lawrence Livermore Laboratory, K-Division and the U.S. Army Engineer Waterways Experiment Station Explosive Excavation Research Laboratory have designed a series of field experiments which have been used in conjunction with numerical modeling calculations to develop such a simulation technique. This program began in FY 1971 as Project Diamond Ore[1] and later expanded into a larger program called Project Essex. Both the experimental[1,2] and calculational aspects of the program[1,3,4] have been emphasized.

The initial goals of Project Diamond Ore included the study of the effects of

burial depth, types of stemming (including stemming vs air stemming), and geologic media on crater size and collateral effects produced by a subsurface detonation of a nuclear cratering device. For convenience, high-explosive field experiments were selected to model nuclear cratering effects. The cratering equivalence of nuclear and high explosive sources was analyzed and established calculationally with the use of the one- and two-dimensional computer codes, SOC and TENSOR. Thus, the calculations provided an interpretative link between high explosive cratering and nuclear cratering. Although we treat only a single nuclear source yield here, the results can be generalized to other yields of interest via standard similitude methods.

This report is a summary of several computer calculations which simulate the cratering process for both nuclear and high explosives emplaced underground in both fully stemmed and unstemmed configurations in Bearpaw shale. It is an update to some results previously reported.[3,4]

In order to define a viable field program, the calculations were restricted to low yield energy sources in a geologic media known to be available for a high-explosive (HE) test program. More explicitly, it was decided to use, as a starting point, the shot parameters of the Pre-Gondola I Charlie detonation of 1966 at Fort Peck, Montana. In this way the calculations could be verified with a well-documented experiment at the same time the experimental program was being designed and conducted.

A nitromethane source was chosen for the initial calculations so that comparisons with the existing experimental Pre-Gondola I results could be made (1966) while the three Diamond Ore Phase IIA experiments were being designed and executed. An aluminized ammonium nitrate slurry (AANS) was selected and used for these field experiments. Detailed measurements in the slurry on these experiments showed that it did not behave in a reproducible manner; that is to say, it detonated like a different explosive in each of the three experiments. This led to extensive additional testing and refinement on a laboratory scale and finally to the decision to develop a gelled nitromethane explosive for experiments to be conducted the following year.[1,5,6] In the meantime, nitromethane was used as the primary energy source for all the HE calculations discussed in this report.

The following calculations were made for a fully-stemmed emplacement hole with the two-dimensional Lagrangian TENSOR code:

1. 20NM12: A 20-ton,* nitromethane (NM) source buried at 12.5 m. This calculation was compared with the Pre-Gondola I Charlie experiment. The Charlie experiment was detonated near optimum burial depth which is defined to be that depth which produces the largest crater volume.

2. 20N12: A 20-ton, hypothetical nuclear (N) source buried at 12.5 m.

3. 10NM12: A 10-ton, NM source buried at 12.5 m.

4. 20NM6: A 20-ton, NM source buried at 6 m.

5. 20NM17: A 20-ton, NM source buried at 17 m.

*One ton of energy represents 4.186 $\times 10^{16}$ ergs or 10^9 cal.

Calculation 10NM12 was carried out with the intent of modeling the effects of the 20-ton nuclear calculation. The choice of the nitromethane yield was based upon kinetic energy coupling found from SOC calculations[3] and qualitative arguments given in Ref. 7. Additional comparisons are shown in the main text and the appendices.

In addition to these stemmed calculations, the coupled TENSOR-PUFL codes were used to perform calculations for the unstemmed (or air stemmed) emplacement hole. The following TENSOR-PUFL calculations will be discussed briefly:

6a. 20N12P50I: A 20-ton, hypothetical nuclear source buried at 12.5 m with an air-stemmed emplacement hole having a 50-cm radius (idealized case).

6b. 20N12P50: A 20-ton, hypothetical nuclear source buried at 12.5 m with an air-stemmed emplacement hole having a 50-cm radius and modeled with friction, heat transfer, and mass addition (non-idealized case).

Cratering Calculations for Stemmed Nitromethane and Nuclear Explosives

Two-dimensional TENSOR[8] code calculations were carried out to simulate fully stemmed cratering detonations in Bearpaw shale (BPS). Twenty-ton NM sources at emplacement depths of 6, 12.5, and 17 m will be discussed. A 10-ton NM source and a 20-ton nuclear source, both buried at 12.5 m, are also included. In order to define the mound and final crater configurations an EJECT calculation was performed on a TENSOR cycle at a relatively late time in the problem, 20 ms or later for these particular geometries.* EJECT is a ballistic throwout code employing slope stability criteria.[10] Many figures included in this report and appendices were produced on the computer using the TENPLT graphics code[10] of which EJECT is one portion.

In all these problems the source region initially is spherical. The input parameters for the nuclear TENSOR problems were obtained from a SOC calculation using a model by Butkovich.[11] For the nuclear calculation, the vaporization radius, pressure, density, and energy density were about 53 cm, 1.3 Mbar, 2.2 g/cm^3, and 1.32×10^{12} ergs/cm^3, respectively. For the high explosive problems, the nitromethane description[12] consisted of an energy density, initial density, Chapman-Jouguet pressure, gamma, and detonation velocity of 0.051 Mbar-cm^3/cm^3, 1.128 g/cm^3, 0.125 Mbar, 2.5386, and 0.6287 cm/μs, respectively. The NM source radii were about 125 and 158 cm for the 10- and 20-ton calculations. The Bearpaw shale description was that reported earlier[3] and is in close agreement with some later measurements.[13]

The initial grid used for calculation 20NM12 is typical and is shown in Fig. 1. The initial Z axis is the axis of cylindrical symmetry with the source region at the origin located 12.5 m below the ground

*Our approach to cratering calculations was similar to that of Terhune, Stubbs, and Cherry.[9]

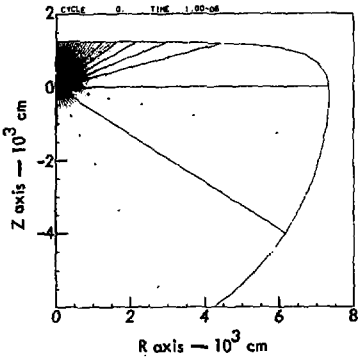

Fig. 1. TENSOR grid for 20NM12.

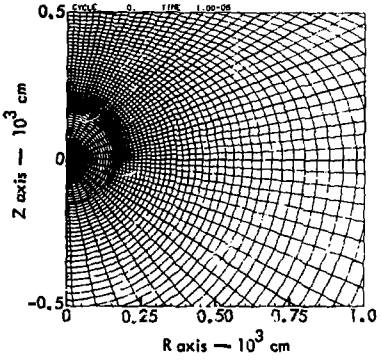

Fig. 2. Enlarged view of TENSOR grid near the center of the source.

surface. The horizontal R axis extends from the origin outward to 80 m in Fig. 1. The c.g.s. system of units was used in these calculations. The dots represent nodal points, intersections of the "K" and "L" lines (logical variables) of the TENSOR grid. The width of zones increases geometrically with increasing radial distance. For this problem the free surface is 12.5 m above the center of the source. The outer radius of the grids used in these problems was greater than 65 m. This value was selected as a practical infinity in order to minimize the effects of nonphysical waves which might be reflected by the finite calculational boundaries at late times. Since the Bearpaw shale media has a sonic velocity of about 2 m/ms, such waves should not return from the outer boundary to the source region before a time of about 65 ms. Note that the zoning is fairly coarse below the source because this is not the region of interest.

Figure 2 shows an enlarged picture of the initial TENSOR zoning (1000 cm × 1000 cm) extending out from the center of the source. Here the nodal points shown in Fig. 1 have been connected by lines and indicate the cross-sectional area of the zones. This 20-ton nitromethane spherical source had a radius of about 158 cm and was enclosed by a "slip" surface. Each zone represents the volume in a quadrilateral revolved about the Z axis.

The slip surface is a special interface used to disconnect adjacent points (in a particular way) in logic (K and L) space. In these problems only compressional or normal motions (no shear or tangential motions) are transmitted across the slip surface and points may "slip" along either side of this movable boundary. The slip surface was utilized around the source region in these problems to retain wavelength resolution at large distances from the source and yet maintain an adequate time step in the region near the source. Without this or a similar device, the small zones near the origin would restrict the time step to a very small value which in

turn would require an excessive amount of computer time. Thus, we have 54 zones (L lines) outside the slip surface vs 18 zones inside the slip surface along K lines.

COMPARISON OF NITROMETHANE AND NUCLEAR SOURCES

In order to compare the nitromethane and nuclear calculations, several plots of the energy transmitted into the Bearpaw shale as a function of time have been included. The total energy transmitted from the source to the Bearpaw shale (BPS) outside of the source region is shown in Fig. 3 as a function of time. An energy scale in tons is shown at the right. The BPS energy rises to a value of about 80% of the total energy (20 tons) and remains constant with time in the nuclear case. For the nitromethane calculations the total BPS energy rises more slowly with time and approaches a value of nearly 90% of the total energy for both the 10- and the three 20-ton cases.

Of more interest in establishing an equivalence between nitromethane and nuclear sources for cratering was the kinetic energy transmitted to the media. A comparison of kinetic energies in the BPS as a function of time is shown in Fig. 4. The energy was released from a nuclear source in less than a microsecond, while the nitromethane source required 200 to 300 ms to completely detonate. The nuclear cavity starts expansion with a pressure on the order of megabars while the HE cavity starts expanding with a cavity pressure on the order of 100 kbar. Thus,

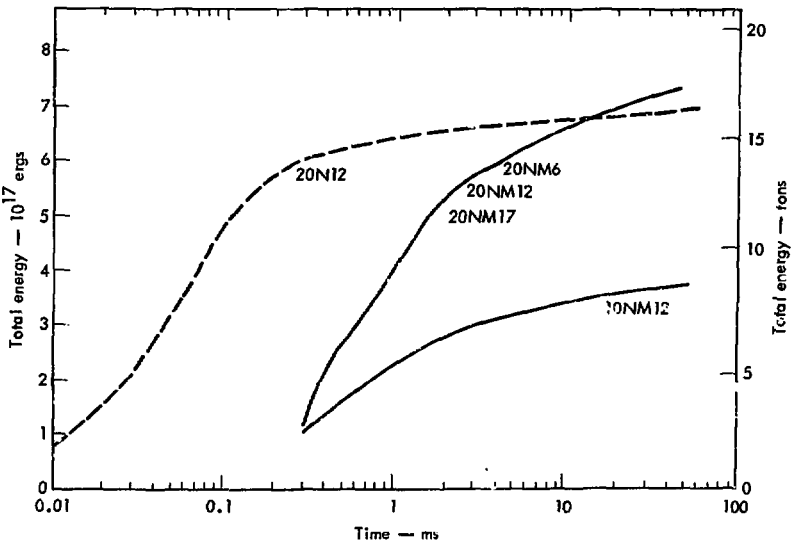

Fig. 3. Total energy transmitted to the BPS outside the source region.

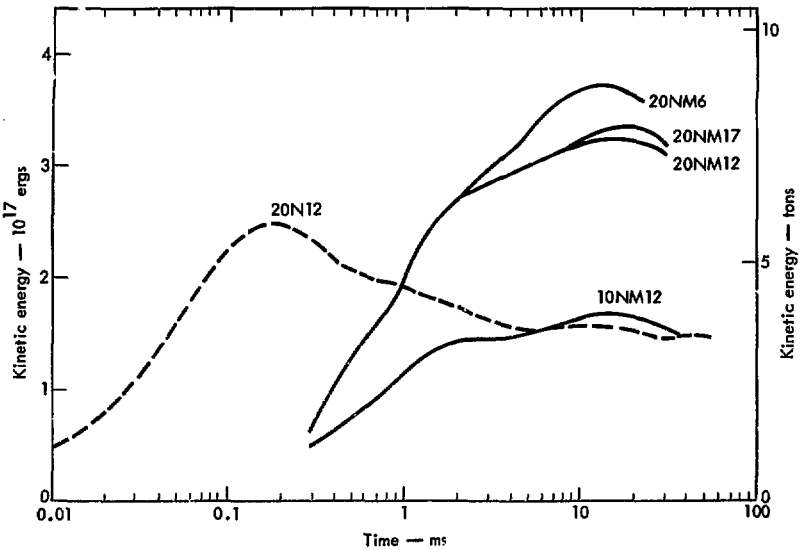

Fig. 4. Kinetic energy in the BPS as a function of time.

equivalence at a very early time was not possible. Likewise, an equivalence for a very shallow cratering shot (less than 4 m) will probably differ from that discussed in this report. For the cratering process it is important that the kinetic energies be comparable at relatively late times, such as 1 to 2 source-to-free-surface transit times (about 5 to 10 ms for the 12.5 m case). The total kinetic energy in the Bearpaw shale due to the nuclear source, peaks at about 2.5×10^{17} ergs (about 30% of the total energy) and about 0.2 ms and then decreases until about 5 to 6 ms, when the shock wave arrives at the ground surface. This behavior is compared with that for the NM problems in Fig. 4. At 5 ms and thereafter, the kinetic energy in the shale due to the 20-ton nuclear source is nearly identical to that of a 10-ton nitromethane source. An increase in kinetic energy due to the rarefaction wave is clearly indicated in the three 20-ton nitromethane problems. The kinetic energies are the same up to the time (about 2 ms) when the shock wave in the 6 m problem (20NM6) reflects from the surface. After this time the kinetic energies in the problems differ. Similarly, the kinetic energies for the 17- and 12.5-m configurations match until about 5 ms when the shock wave from the latter strikes the surface.

This increase in kinetic energy as the shock wave was reflected off the free surface was even more pronounced in the kinetic energy of the mound material alone. Mound kinetic energies were calculated

using the EJECT code described below. At 20 ms the mound kinetic energies for *10NM12 and 20NM12 were* about 10% and 150% higher, respectively, than the mound kinetic energy for 20N12. Thus, the 10-ton nitromethane calculation looked quite similar to the 20-ton nuclear calculation. A further discussion will follow (see Fig. 17).

Figure 5 defines the crater nomenclature. The parameters used in our discussion include the apparent crater radius R_A; the apparent crater lip radius, R_{AL}; the

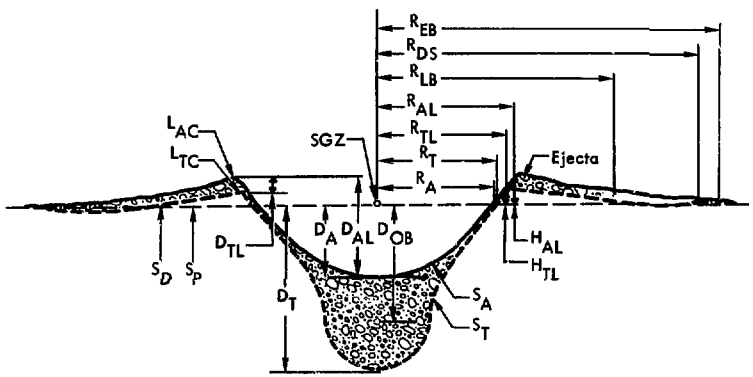

D_A Maximum depth of apparent crater below preshot ground surface measured normal to the preshot ground surface.*

D_{AL} Depth of apparent crater below average apparent crater lip crest elevation.

D_{OB} Normal depth of burst (measured normal to preshot ground surface).

D_T Maximum depth of true crater below preshot ground surface.

D_{TL} Depth of true crater lip crest below apparent crater lip crest.

Ejecta Material above and or beyond the true crater and includes: (1) foldback; (2) breccia — ballistic trajectory; (3) dust — aerosol transport; etc.

H_{AL} Apparent crater lip crest height above preshot ground surface.

H_{TL} True crater lip crest height above preshot ground surface.

L_{AC} Apparent crater lip crest.

L_{TC} True crater lip crest.

R_A** Radius of apparent crater measured on the preshot ground surface.

R_{AL} Radius of apparent lip crest to center.

R_{DS} Outer radius of displaced surface.

R_{EB} Radius of outer boundary of continuous ejecta.

R_{LB} Outer radius of true lip boundary.

R_T Radius of true crater measured on the preshot ground surface.

R_{TL} Radius of true lip crest to center.

S_A Apparent crater surface, e.g. rock-air or rubble-air interface.

SGZ Surface ground zero.

S_D Displaced ground surface.

S_P Preshot ground surface.

S_T True crater surface, e.g. rock-air or rock rubble interface.

V_A Volume of apparent crater below preshot ground surface

V_{AL} Volume of apparent crater below apparent lip crest.

V_T Volume of true crater below preshot ground surface.

V_{TL} Volume of true crater below true crater lip crest.

* All distances, unless specified otherwise, are measured parallel or perpendicular to preshot ground surface.

** The radius measurements pertain only to single charge craters and represent average dimensions. If crater shape deviates substantially from circular, the direction of measurement must be specified. An average radius value can also be determined by dividing the plan area by π and taking the square root.

Fig. 5. Crater nomenclature.

apparent crater volume, V_A; the apparent crater depth, D_A; the apparent crater lip height, H_{AL}; and the apparent crater lip volume, V_{AL}.

The EJECT code has been developed to use the variables in the TENSOR grid at a fixed time (cycle) and to calculate an ejecta profile and final crater configuration. The times chosen for linking EJECT and TENSOR depend primarily upon the depth of burial and the sonic velocity of the media. This point will be examined in more detail later. Figure 6 shows one of the results of an EJECT calculation for the nuclear problem at 30 ms. The mound boundary is shown as the line between the dotted region or mound and the cross-hatched region. The dots denote TENSOR nodal points. The mound is defined to consist of those zones having upward velocities sufficient to raise them above the original ground surface. The remaining material underneath the "mound" is cross-hatched for zones which are cracking (zones which are currently undergoing failure), cracked (zones which have failed at an earlier time but are not currently undergoing failure), or elastic (zones which have not failed). The motion of each zonal mass was treated as a projectile in a gravitational field moving independently of the other masses. This ejecta was then tabulated according to its ballistic range into a histogram having intervals of 50 cm. The ejecta was then allowed to bulk according to an empirical bulking factor,[3] and the resulting ejecta profile was superimposed upon the mound boundary or preshot ground surface as appropriate. The result appears in Fig. 6.

The slopes appearing in this figure are, of course, unstable. Consequently, mass was allowed to tumble downward until an apparent crater profile with stable slopes was obtained, the slope stability criterion at a given radius being expressed in terms of the slope of a hyperbola having an asymptote equal to the observed slope stability angle for BPS.[14] The apparent crater profile that results from this calculation appears in Fig. 7. Similar

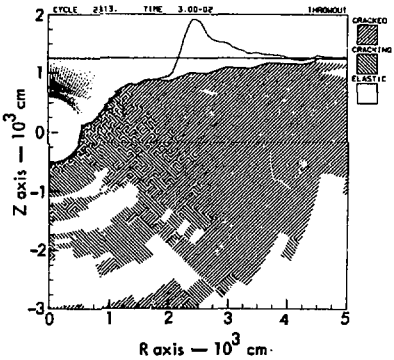

Fig. 6. EJECT ballistic calculation for 20N12 at 30 ms.

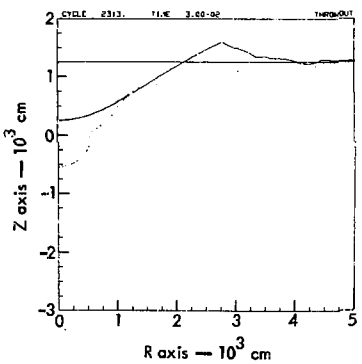

Fig. 7. Apparent crater at 30 ms.

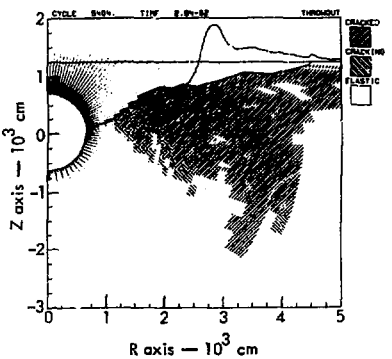

Fig. 8. EJECT ballistic calculation for 20NM12 at 29.4 ms.

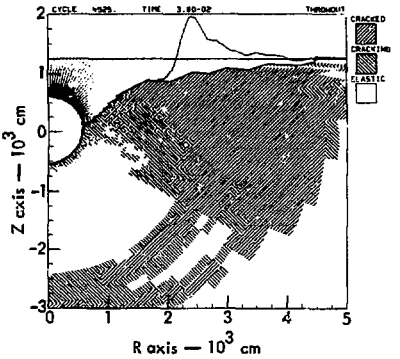

Fig. 10. EJECT ballistic calculation for 10NM12 at 30 ms.

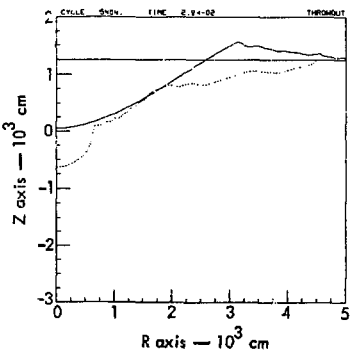

Fig. 9. Apparent crater at 29.4 ms.

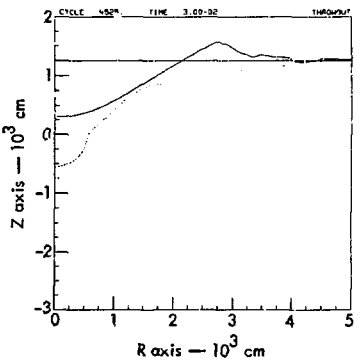

Fig. 11. Apparent crater at 30 ms.

results are shown in Figs. 8 through 15 for the 20NM12, 10NM12, 20NM6, and 20NM17 configurations. Additional comparisons of the crater and mound behavior are shown later in the report (Figs. 16 through 24 and in Table 2). Input parameters for the EJECT calculations were the bulking factor (1.2), slope stability angle (35 deg), gravitational constant (980 cm/s^2), distance between hyperbola and asymptote on axis (500 cm), and a depth to define the radius of continuous ejects (5 cm). Future improvements planned for the EJECT code include treating cavity rebound (discussed later) and the effects of air friction.[10]

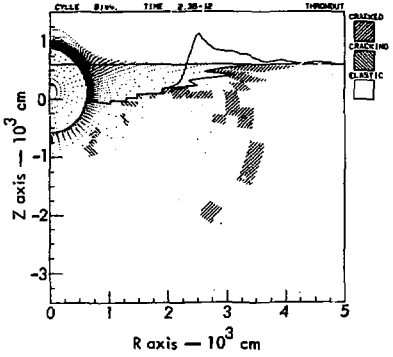

Fig. 12. EJECT ballistic calculation for 20NM6 at 23.5 ms.

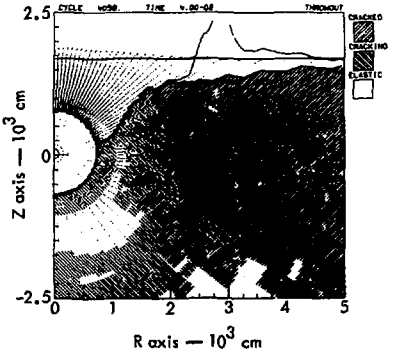

Fig. 14. EJECT ballistic calculation for 20NM17 at 40 ms.

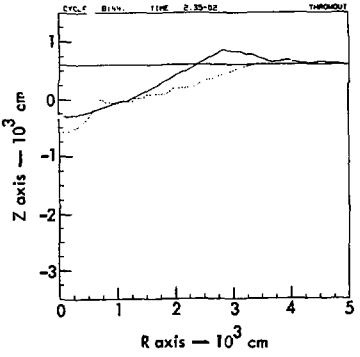

Fig. 13. Apparent crater at 23.5 ms.

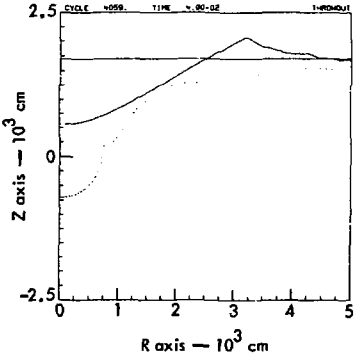

Fig. 15. Apparent crater at 40 ms.

The TENSOR code was used to dynamically model the two-dimensional stress wave propagation. Once the velocity field was established in the mound region, the EJECT code was used to ballistically calculate an EJECT profile and final crater configuration. Since the proper link time for an EJECT calculation was not known a priori, a series of TENSOR times (cycles) were used. A proper link time was assumed to have been found when the various crater variables ceased to change significantly with additional TENSOR problem time. The time required for this

to occur was not found to be simply a linear function of emplacement depth, but rather depended upon the yield, geology, configuration, sound velocity, and depth. The proper link time represents the time required for the velocity field to become established in the mound region and consequently depends upon the interaction of many variables.

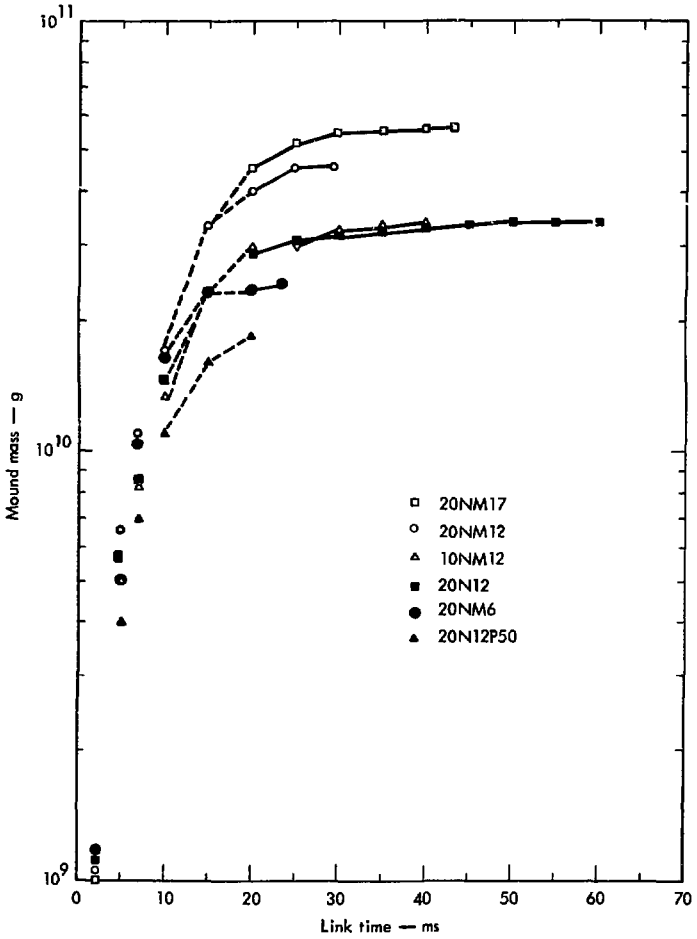

Fig. 16. Mound mass vs link time.

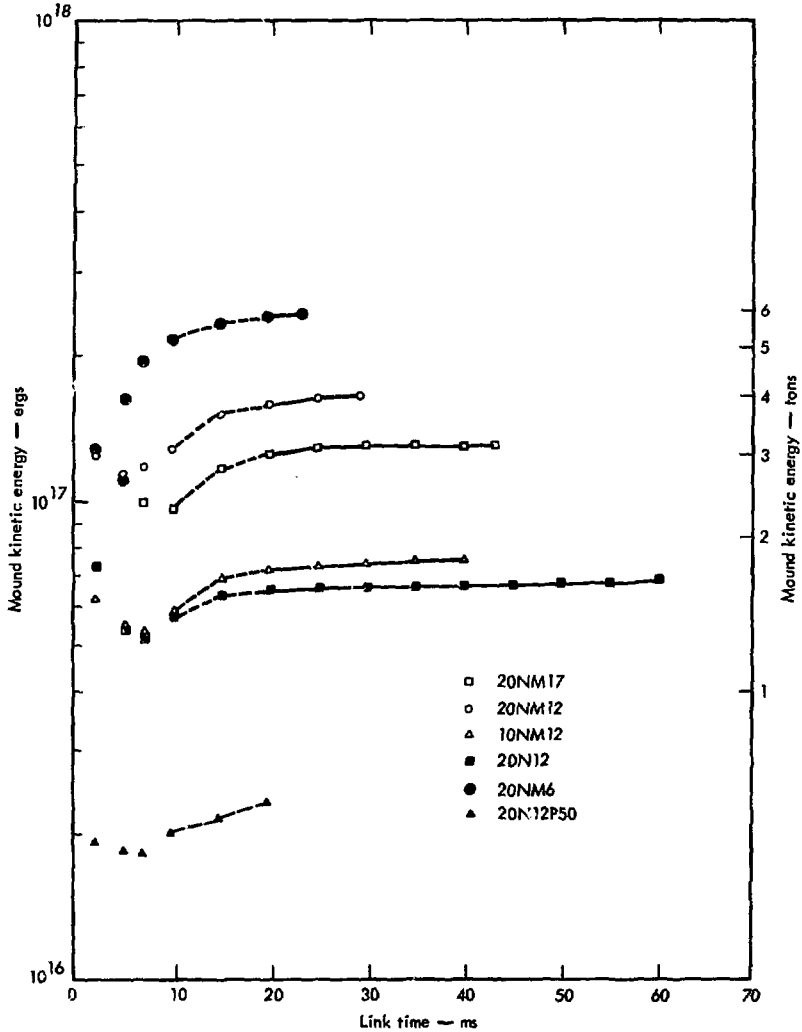

Fig. 17. Mound kinetic energy vs link time.

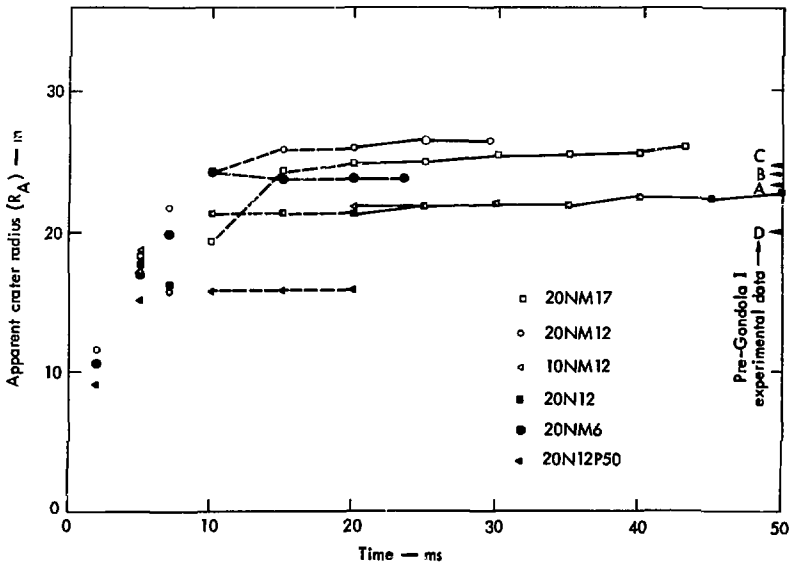

Fig. 18. Apparent crater radius vs link time.

The following series of figures (16 to 24) demonstrate how several crater parameters, calculated with EJECT, change with the TENSOR problem time. From these figures, it was concluded that the dynamical treatment with *TENSOR* for 20 ms was sufficient to guarantee meaningful EJECT calculations for all configurations. Dotted lines have been used to connect points calculated before 20 ms to indicate that these EJECT calculations were performed too early in the TENSOR problem time history. Some of these points were calculated at times before the stress wave initially impinged on the free surface and therefore were not physically realistic for an EJECT calculation.

Figure 16 shows the mound mass calculated with the EJECT code at various link times. The mound mass for each problem increased rapidly until about 20 to 30 ms. The mound masses for 20N12 and *10NM12 were nearly equal. The* calculation with the greatest depth of burst (DOB) 20NM17, has the largest mass. It was followed by the so-called "optimum depth of burst," 20NM12 calculation. The calculation 20NM06 has the smallest mound mass of the stemmed calculations. An unstemmed nuclear problem 20N12P50, calculated using the TENSOR-PUFL code on a 50-cm-radius hole, was included for comparison. This calculation will be discussed in a later section.

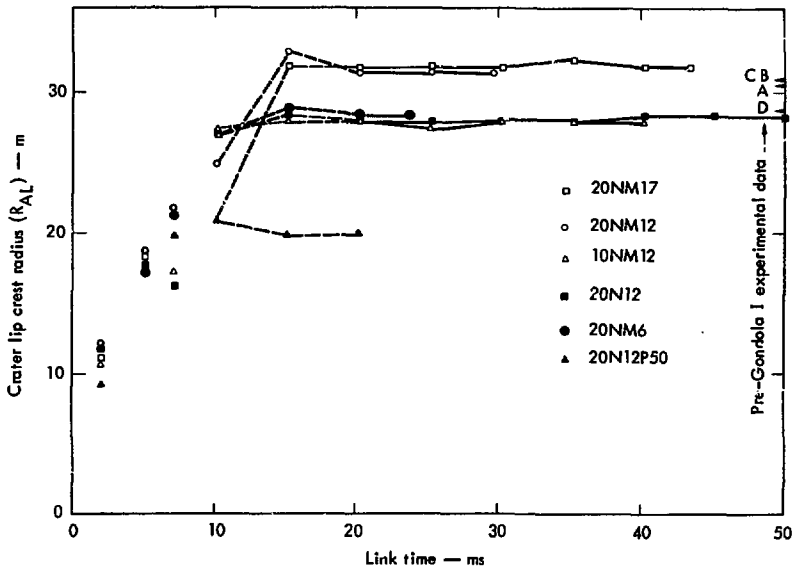

Fig. 19. Apparent crater-lip radius vs link time.

Figure 17 shows similar plots of the mound kinetic energy (ergs or tons) as calculated with the EJECT code at various link times. Figure 17 may be compared with Fig. 4. The mound kinetic energies increased until about 20 ms while the velocity field is being established in the mound region. The calculation with the shallowest depth of burst (DOB), 20NM6, has the largest mound kinetic energy (nearly 30% of its total energy). Calculation 20NM12 has about 20% of its total energy in mound kinetic energy. The results for the 20-ton nuclear source and the 10-ton nitromethane source differ by about 10%.

In Fig. 18, the apparent crater radius, R_A, is shown for various times based on EJECT calculations. The apparent crater radius is taken at the intersection of the final crater with the original ground surface (see Fig. 5). These radii appear to remain essentially constant after 15 ms. The apparent crater radius for calculation 20NM12 is largest and radii for 20N12 and 10NM12 are nearly the same. Experimental results for the Pre-Gondola I series (about 20 tons) are shown at the right hand margin (A = Alfa, B = Bravo, C = Charlie, and D = Delta; also see Table 3). Similar results are shown in Fig. 19 for the apparent lip radii R_{AL}.

The apparent crater volume calculated using EJECT is shown at various times in Fig. 20. The calculation at optimum depth-of-burst, 20NM12, has the largest

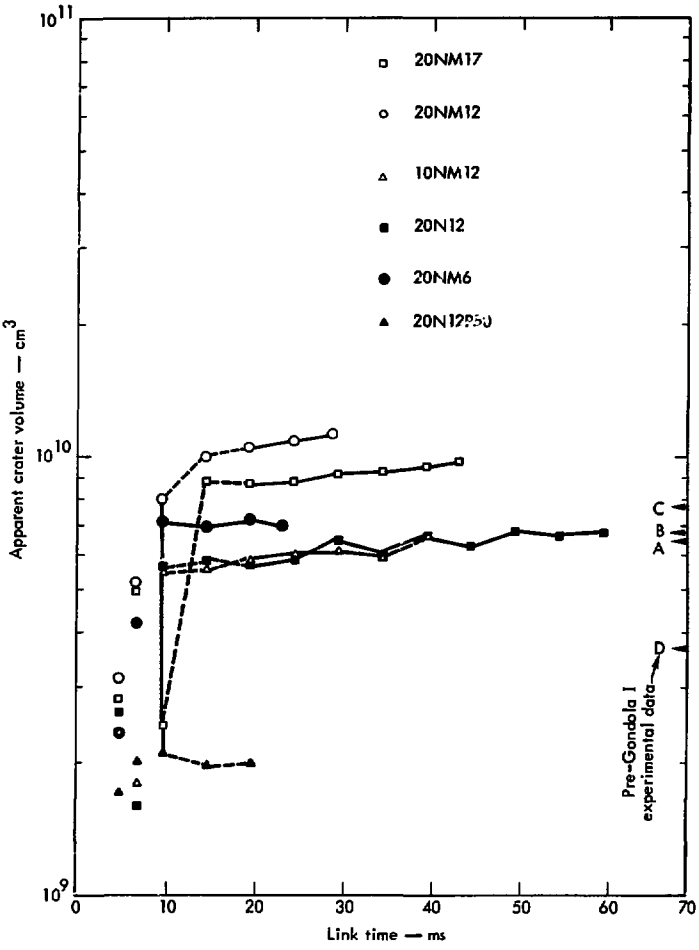

Fig. 20. Apparent crater volume vs link time.

crater volume which is consistent with the definition of optimum depth. The crater volumes for 20N12 and 10NM12 are nearly equal. The values for crater volume do not reach these final values until after 15 ms. Some experimental results are included for comparison on the right side of Fig. 20.

The axial momentum of the mound (along the vertical Z axis) is shown in Fig. 21. The values of axial momenta do not reach a constant value until after 20 ms.

Figure 22 shows the apparent crater depth D_A calculated with the EJECT code. It appears to be easier to match experiment with calculated crater radii R_A and

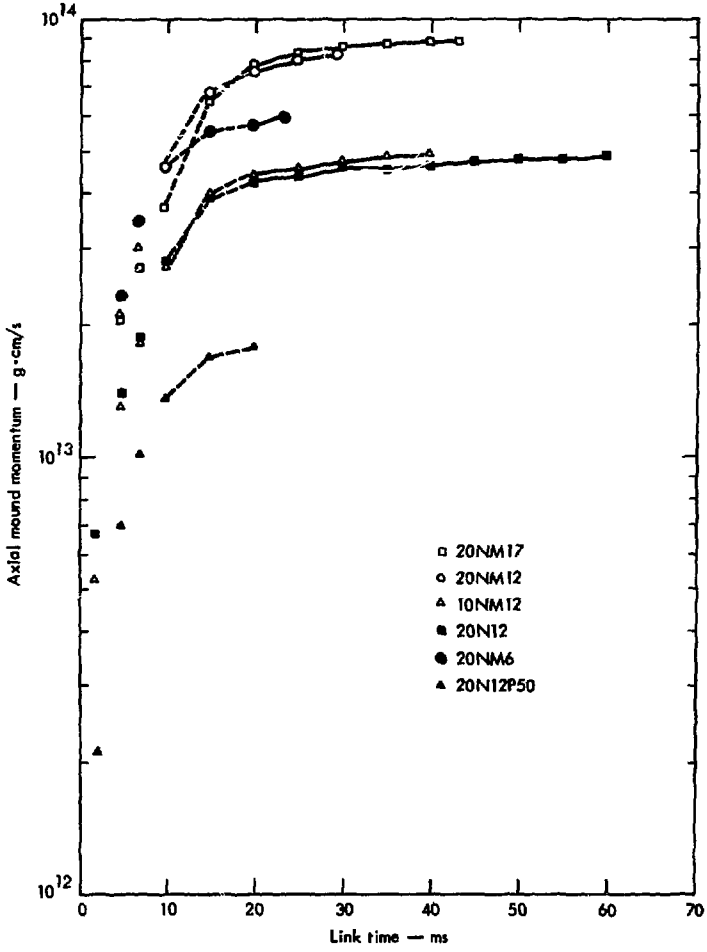

Fig. 21. Axial mound momentum vs link time.

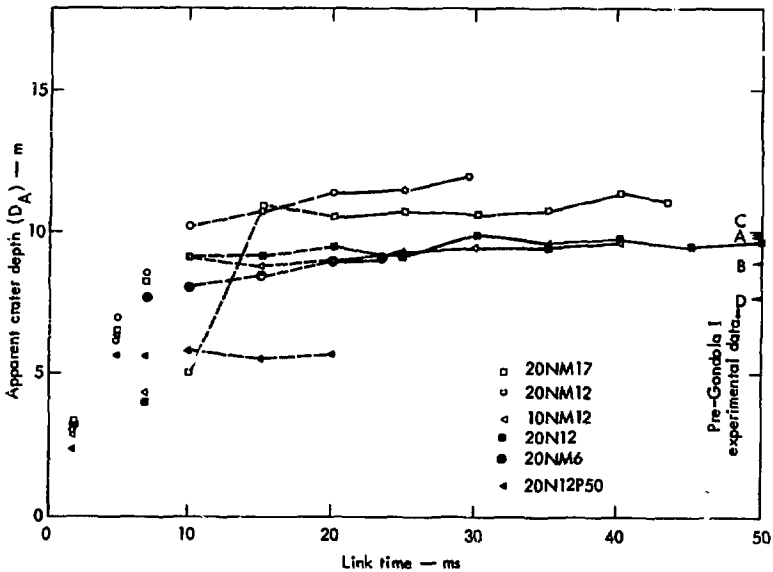

Fig. 22. Apparent crater depth vs link time.

R_{AL} than with either the apparent crater depth D_A and apparent crater lip height, H_{AL}. Calculation 20NM12 has the deepest crater. Calculations of apparent lip height H_{AL} are shown in Fig. 23.

The apparent lip volumes are shown in Fig. 24. These volumes are larger than the apparent crater volume in Fig. 19 due to the addition of the crater lip. Calculations 20NM12 and 20NM17 have the largest apparent lip craters. Experimental values reported for the Pre-Gondola series are also shown on the right side of Fig. 24.

At least three conclusions were drawn from Figs. 16 through 24. First, they indicate that these TENSOR problems should be run to at least 20 ms so that the velocity field will stabilize and so that an EJECT cratering calculation will be meaningful. Secondly, in terms of mound and cratering behavior, the 20-ton nuclear problem (20N12) is very nearly the same as the 10-ton nitromethane problem (10NM12) for the fully-stemmed source buried at 12.5 m. Thus, the high explosive source (NM) is about twice as efficient as the nuclear source for excavation in Bearpaw shale in these configurations.* Thirdly, the air-stemmed

*Theodore Butkovich has pointed out that this conclusion is similar to a conclusion he drew based on one-dimensional calculations in a Rhyolite media.[15]

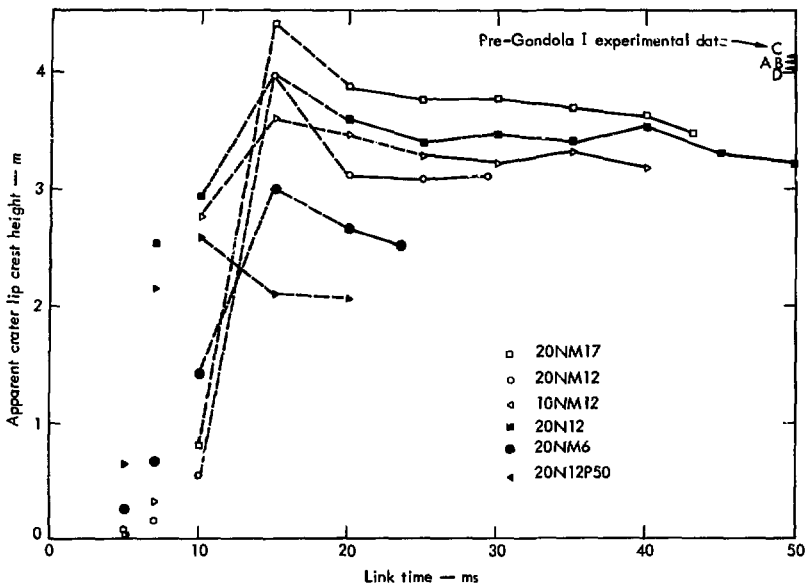

Fig. 23. Apparent lip height vs link time.

Table 1. A comparison of crater parameters at 20 ms. Percentages are relative to 20N12.

	20N12	10NM12	20NM12	20NM6	20NM17	20N12P50
Mound mass, g	2.86×10^{10} —	2.98×10^{10} (+4%)	4.00×10^{10} (+40%)	2.36×10^{10} (-17%)	4.5×10^{10} (+59%)	1.84×10^{10} (-36%)
Mound kinetic energy, ergs	6.46×10^{16} —	7.15×10^{6} (+11%)	1.61×10^{17} (+150%)	2.41×10^{17} (+270%)	1.26×10^{17} (+95%)	2.33×10^{16} (-64%)
Apparent crater radius (R_A), m	21.2 —	21.7 (+2%)	25.8 (+22%)	23.7 (+12%)	24.8 (+17%)	15.7 (-26%)
Apparent crater depth (D_A), m	9.48 —	8.97 (-5%)	11.4 (+20%)	9.00 (-5%)	10.5 (+11%)	5.61 (-41%)
Apparent crater volume (V_A), cm^3	5.80×10^{9} —	5.90×10^{9} (+2%)	1.05×10^{10} (+81%)	7.15×10^{9} (+23%)	8.69×10^{9} (+50%)	1.97×10^{9} (-66%)
Apparent lip radius (R_{AL}), m	27.8 —	27.8 (+0%)	31.3 (+13%)	28.3 (+2%)	31.8 (+14%)	19.7 (-29%)
Apparent lip height (H_{AL}), m	3.57 —	3.45 (-3%)	3.11 (-13%)	2.65 (-26%)	3.86 (+8%)	2.04 (-43%)
Apparent lip crater volume (V_{AL}), cm^3	1.25×10^{10} —	1.21×10^{10} (-3%)	1.83×10^{10} (+46%)	1.26×10^{10} (+1%)	1.83×10^{10} (+46%)	3.86×10^{9} (-69%)
Axial mound momentum, g·cm/s	4.23×10^{13} —	4.47×10^{13} (+6%)	7.61×10^{13} (+80%)	5.71×10^{13} (+35%)	7.78×10^{13} (+84%)	1.78×10^{13} (-58%)

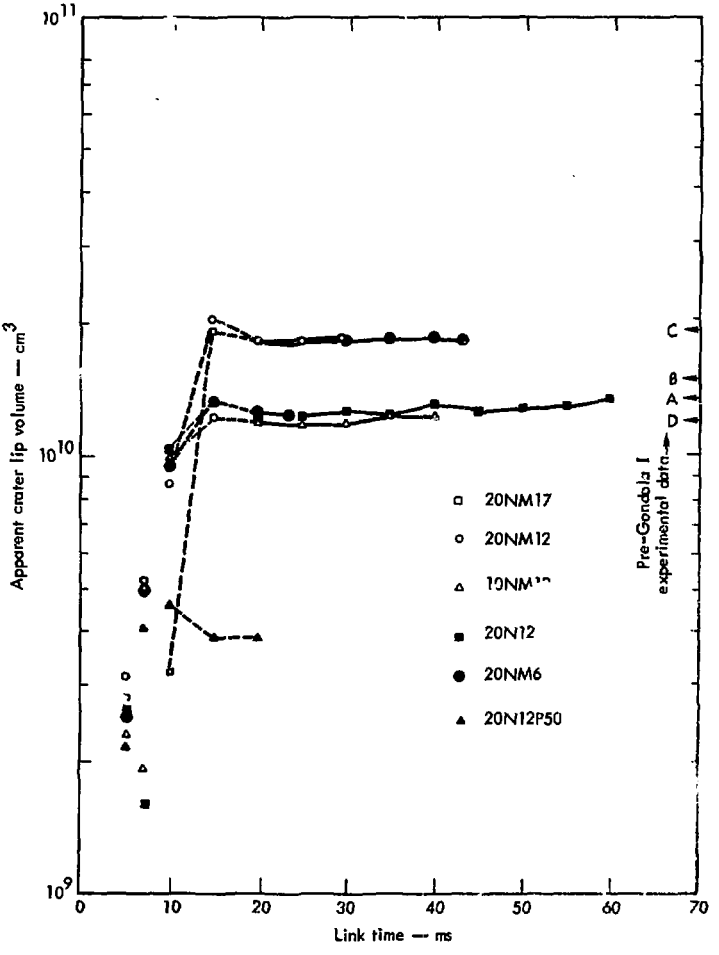

Fig. 24. Apparent lip volume vs link time.

nuclear source produced a significantly smaller crater than any other configuration (this calculation is discussed later). Further comparisons between 20N12 and 10NM12, including velocity fields, pressure fields, ballistic and cratering calculations, are displayed graphically in the appendices.

Table 1 is a comparison summary of the previous figures at 20 ms. This time was chosen so that all six problems could be compared at the same time. The percentages shown in parentheses compare each calculation with the 20N12 calculation. The 20-ton nuclear source is most nearly like the 10-ton nitromethane source at 12.5 m in terms of cratering.* The calculation 20NM12 seems to be the nearest one to "optimum" DOB in terms of earth excavation.

COMPARISON OF 20NM12 AND PRE-GONDOLA I CHARLIE

It is important to compare calculation with experiment. Values calculated from 20NM12 with the EJECT code at 30 ms are compared with data reported for the Charlie crater in Table 2.[17] EJECT calculations which employed both the conical and hyperbolic models† are included for comparison. The yield and DOB for the 20NM12 calculation were about +4% and -3% of those for the Charlie event, respectively. The radius of continuous ejecta was defined as being 5 cm above the ground surface. The percentage differences are listed in parentheses. The agreement appears to be close except for the crater depth, lip height, and apparent crater volume. The average lip heights of 3.4 and 3.1 m are lower than the reported maximum or minimum lip heights of 5.2 and 3.8, respectively. The crater depth calculation probably would be improved if a "cavity rebound" treatment[9] were added to EJECT. This would improve both the calculated values for depth and apparent crater volume. Attempts at an improved modeling of this aspect of EJECT calculation are planned for the future. All these calculated values depend on the parameter used for the constant bulking factor (1.2) and the slope stability angle (35 deg) in the EJECT calculation. The sensitivity of the EJECT model to these parameters is discussed in Ref. 10.

Calculated and measured crater profiles are summarized in Fig. 25. There is some variation in the four observed crater cross sections. The differences may be attributed to geological variations in various directions. The numbers quoted in Table 2 were average values. As described earlier, the calculated profile was the result of allowing the ejecta to "tumble" downward until stable slopes

*Since the mound kinetic energy is about 10% higher for 10NM12 than 20N12, it might be concluded that 9 rather than 10 tons of nitromethane should have been used to produce a better equivalence. However, the effects of shock vaporization of water (above about 100 kbar) in the saturated Bearpaw shale media has not been included in the two-dimensional modeling. One-dimensional calculations, like those reported earlier,[3] indicate about a 10% enhancement in kinetic energy when the "water boost" model is utilized to treat the nuclear source in Bearpaw shale.[16] Thus, 10 tons of nitromethane is the cratering equivalent of 20 tons of nuclear energy for the configurations and media discussed in this report.

†Initially in the development of EJECT a conical crater shape was used. Later the hyperbolic crater shape was introduced which gives better values for crater depth.

Table 2. Comparison of Pre-Gondola I Charlie with 20NM12 at 29.4 ms.

	Experiment	Conical crater calculation	Hyperbolic crater calculation
	Pre-Gondola I: Charlie	20NM12	Same
Yield, tons	19.26	20[a]	Same
Depth of burst, m	12.95	12.5[a]	Same
Apparent radius (R_A), m	24.8	25.8 (+4%)	26.3 (+6%)
Apparent depth (D_A), m	9.91	15.5 (+56%)	12.0 (+21%)
Apparent lip radius (R_{AL}), m	31.0	31.3 (+1%)	31.3 (+1%)
Average lip height (H_{AL}), m	4.4	3.4 (-23%)	3.1 (-30%)
Radius of continuous ejects, m	89.6	94.3 (+5%)	Same
Apparent crater volume, m^3	8.16×10^3	1.11×10^4 (+36%)	1.13×10^4 (+38%)
Apparent lip volume, m^3	1.97×10^4	1.94×10^4 (-2%)	1.86×10^4 (-6%)

[a]Input values for the TENSOR calculation.

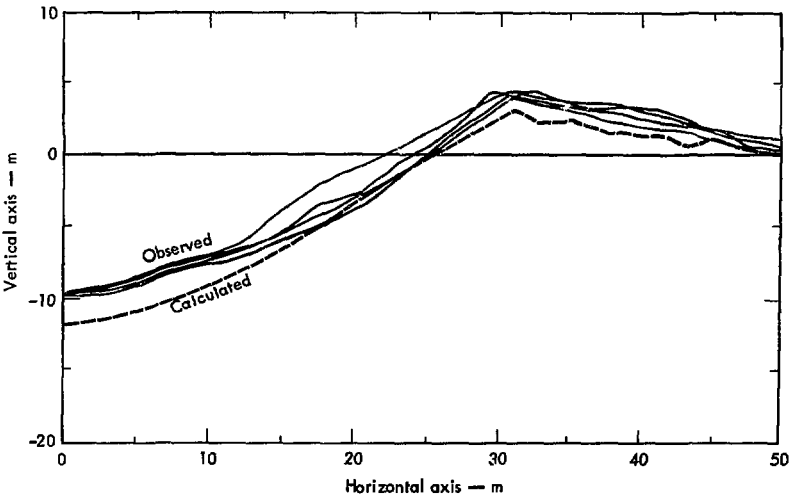

Fig. 25. Comparison of calculated and measured (pre-Gondola I Charlie) crater profile.

were achieved. Within the crater region the profile was artificially constrained to conform to the shape of a hyperbola with a 35-deg asymptote. As very little mass was involved, the effect of hyperbolic constraint was primarily cosmetic, significantly altering only the calculated apparent crater depth (see Table 2). Also shown in Table 2 are the results of a conical crater calculation in which the hyperbolic constraint was removed. Physically, the hyperbolic craters usually are observed and arise from two effects. The first effect is the inward radial momentum of the ejecta as it tumbles down the crater slopes. The second is the cavity rebound effect which occurs because the region below the cavity is still compressed at the time of linking with the EJECT code. At later times, this material will be restored to some fraction of the original zonal volume, depending upon the hysteresis in the loading-unloading curve for the material. Because of the latter effect, the calculated crater volumes can be expected to be somewhat larger than those actually observed.

Calculations for Unstemmed Explosives

In order to treat a particular class of gas dynamic calculations with pipe flow, the quasi-one-dimensional PUFL code[18] and the two-dimensional TENSOR code[8] have been coupled together as TENSOR-PUFL.[19] Each code retains its integrity, but they interact periodically, each providing a boundary condition for the other. Figure 26 shows a portion of a TENSOR-PUFL grid at the time the calculation was begun. The boundary between the TENSOR and PUFL regions, near the Z axis, represents the ground-air interface in the open hole. The entire source is also included in the PUFL grid. At any given time, only one of the codes is operating on the computer. TENSOR, having larger time steps, typically runs a single cycle (time step), PUFL runs several cycles, then TENSOR runs, etc. In this alternating process, as control is passed from PUFL to TENSOR, PUFL pressures are used as a boundary condition (pressure vs time and position) along the common boundary between the TENSOR and PUFL grids. Later when control is passed back from TENSOR to PUFL, TENSOR provides PUFL with a boundary condition (displacement vs time and position). In this manner both the

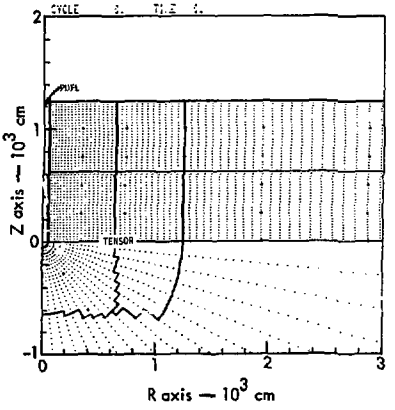

Fig. 26. TENSOR-PUFL grid.

gas flow in the open hole under consideration here and ground motions may be modeled in a TENSOR-PUFL treatment.

The TENSOR-PUFL calculations have proved to be considerably more tedious than the TENSOR calculations. This new application of TENSOR-PUFL has required considerable modification of both computer codes. In addition, the unstemmed calculations (TENSOR-PUFL) run slower on the computer than the stemmed calculations (TENSOR) due to the increased complexity. Here we will discuss two calculations for a hypothetical 20-ton nuclear source buried at 12.5 m (about 41 ft). A hole size with a 50-cm radius (or about 20 in.) was input in these air-stemmed calculations. The problems were run both with (non-idealized, 20N12P50) and without (idealized, 20N12P50I) the friction, heat transfer, and mass addition coefficients to observe their calculational effects. Some comparisons for these calculations are included here even though only one of them has been run sufficiently long (at least 20 ms for a 12.5 m configuration) for an EJECT calculation to predict a realistic crater size.* Some geometrical considerations associated with the TENSOR-PUFL grids have required an extensive generalization of the EJECT code. Since relatively very little mass is included in the PUFL region (even with mass addition) and each zone has only an axial velocity, the PUFL mass was omitted in the EJECT calculations for the unstemmed configurations.

For these initial TENSOR-PUFL calculations, simple ideal gas descriptions have been used for both the source and air regions in the PUFL code. The material description input to the TENSOR code is that described in our earlier report on Bearpaw shale[3] and is the same as was used for the calculation of stemmed sources. Originally all the energy was input as internal energy in the source region of PUFL. As this region expands the pressure profile calculated by the PUFL code is used as a pressure profile on the TENSOR boundary and energy is transferred through P·dV work from PUFL to TENSOR.

The TENSOR portion of the grid is shown in Fig. 26. The center portion near the vertical axis is the unstemmed hole and source region represented by the PUFL code. Some initial PUFL parameters are:

	Source	Air
Density:	4.4×10^{-2} g/cm^3	10^{-3} g/cm^3
Pressure	$6.4 \times 10^{+11}$ ergs/cm^3	10^6 ergs/cm^3 (1 bar)
Zone size:	1 cm	20 cm
Number of zones:	100	60
Gamma:	1.5	1.2

These conditions were chosen to represent the vaporization cavity, which is estimated to be present at about 70 $W^{1/3}$ μs where W is the source energy in kilotons.[11] For this calculation, 0.020 kt represents a time of about 19 μs. Some differences in the initial conditions might exist if an earlier time were represented (e.g., 1 μs). The PUFL code has been modified so that PUFL zones are removed from the problem when they travel up the open hole

*A comparison of the idealized case (20N12P50I) with the non-idealized case (20N12P50) at 5 ms showed that significantly more energy had escaped up the open hole in the former case. In addition, 20N12P50 had coupled about 50% more kinetic energy into the BPS. Since the ideal case appeared to have only academic interest, only the non-ideal case was run to 20 ms.

and pass beyond the free surface represented by the TENSOR code. As these zones are deleted, the code tabulates their energies, momenta, and masses.

Figure 27 shows the energy transfer to the TENSOR grid (all Bearpaw shale) as a function of time in the idealized TENSOR-PUFL problem, 20N12P50I, without friction, heat transfer, or mass addition parameters. At 5 ms about 1.7×10^{17} ergs of energy (20% of the total energy) has been transferred into the shale. Figure 28 shows the nonidealized problem 20N12P50 run with friction, heat transfer, and mass addition. Here about 2.2×10^{17} ergs (or 26% of the total energy) have been transferred to the shale at 5 ms. The kinetic energy in the shale at 5 ms is about 50% higher for the nonideal case than the ideal case. In this calculation, at 5 ms, nearly 60% of the total energy had gone up the open hole and was lost from the system.

Figure 29 shows the effect of these parameters on the calculated arrival times up the open hole. The idealized case shows an average shock velocity of about 7.0 cm/μs vs about 6.2 cm/μs (or about 10% less) in the nonidealized case. The slope of the arrival time curve or shock velocity (in cm/μs) is indicated at several times along the curve. The top of the hole is at 12.5 m.

The attenuation of peak pressure with axial distance is indicated in Figs. 30 and 31. Peak pressures are about equal at the

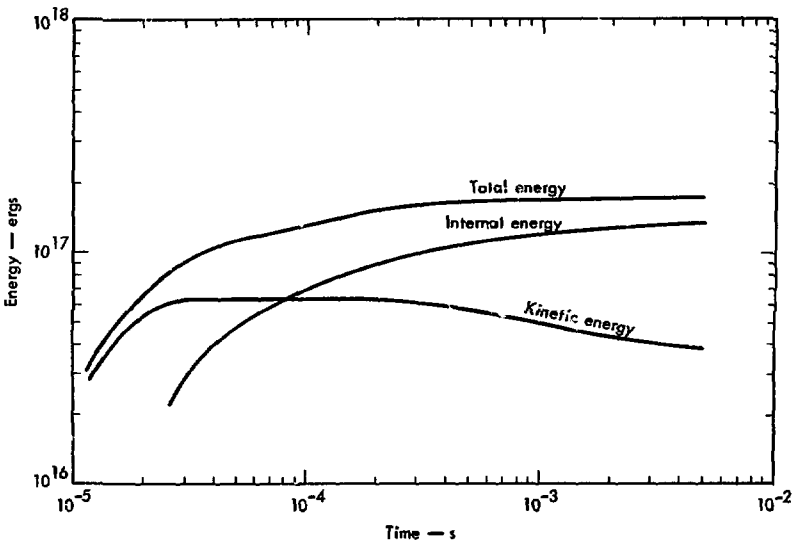

Fig. 27. Energy transferred to BPS and 20N12P50I (idealized).

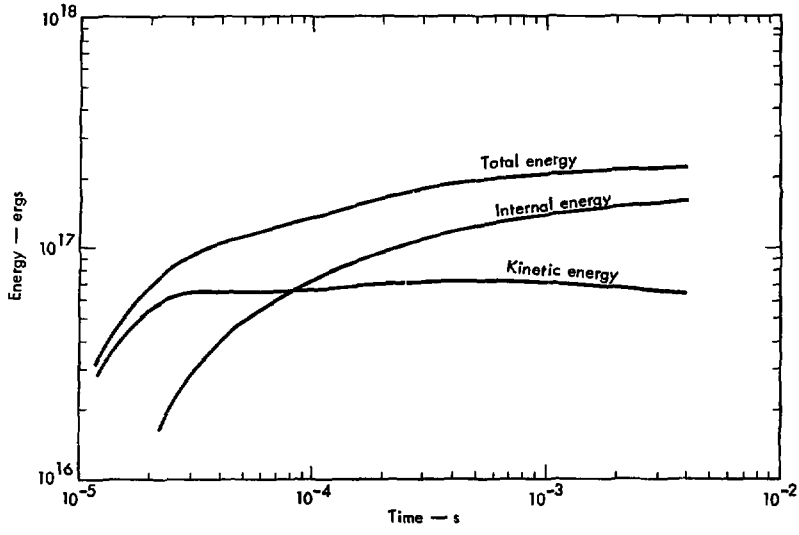

Fig. 28. Energy transferred to BPS and 20N12P50 (non-idealized).

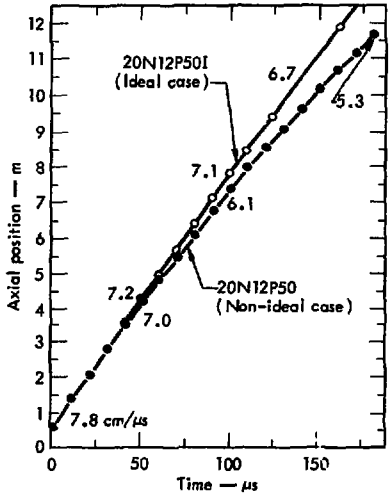

Fig. 29. Shock arrival times in the open hole (PUFL region).

4 m position in both cases. In the ideal case the peak pressure has fallen to about 39 kbar at 12 m while in the nonidealized case it is about 23 kbar at 12 m.

At the present time there is some latitude in the choice of parameter values for the friction, heat transfer, and mass addition. It is possible that a set or sets of parameters may be found that match arrival time measurements for a particular experiment in the open hole while the calculated pressures may not necessarily match the experimental pressures. Thus, it appears to be worthwhile to attempt both time-of-arrival and pressure history measurements on future unstemmed cratering shots. It is desirable to have a calculation which matches the arrival time as well as the pressure history measurements in the air-stemmed cratering configuration.

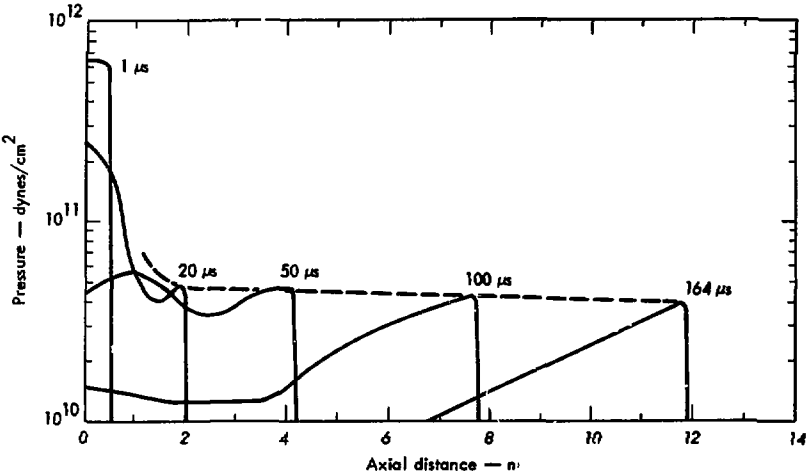

Fig. 30. Pressure profiles for 20N12P50I.

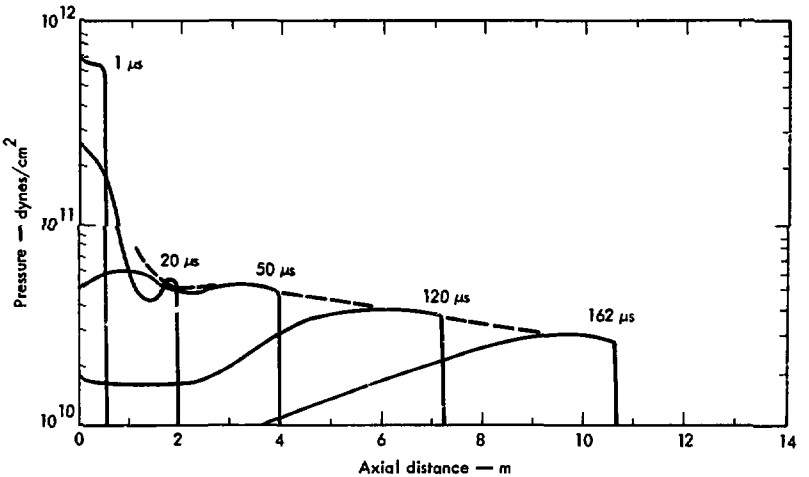

Fig. 31. Pressure profiles for 20N12P50.

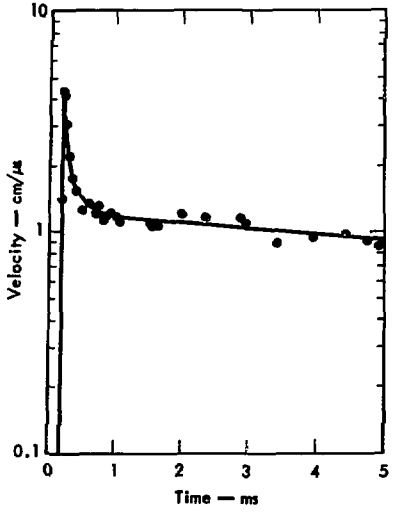

Fig. 32. Gas velocity near surface for 20N12P50.

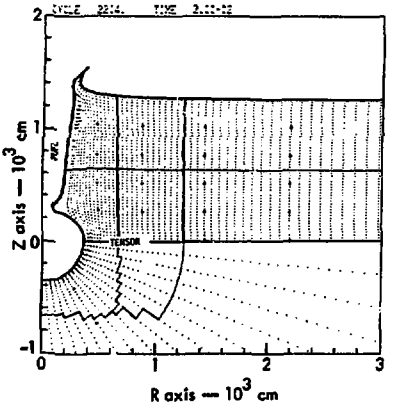

Fig. 33. TENSOR-PUFL grid for 20N12P50 at 20 ms.

Figure 32 shows the velocity of material near the open hole for the 20N12P50 calculation, about 50 cm b[illegible] the original free surface. The peak [illegible]city from hydrodynamic motion, 4 cm/μs, arrived at about 0.2 ms and dropped to a value near 1 cm/μs.

The 20-ton nuclear case with a 50-cm radius (20N12P50) was run out to 20 ms. Figure 26 shows a portion of the initial TENSOR grid. The empty region adjacent to the vertical Z axis represents the PUFL region. Figure 33 shows this same TENSOR grid at 20 ms with the PUFL region significantly enlarged as the result of the expanding gases. The ground shock wave has produced a closure effect between 2 and 4 m while the remainder of the hole has expanded in radius.

Figure 34 shows the mound boundary, cracked regions, and the ejecta profile for the unstemmed calculation with friction, mass addition, and heat transfer. Figure 35 shows results from the ballistic calculation and the final crater configuration. This crater is significantly smaller than any of the fully-stemmed calculations. Other comparisons between this air-stemmed calculation and the fully-stemmed calculations have been labelled 20N12P50 in Figs. 16 to 25 and Table 1 in the previous section for comparison. A comparison of either mound kinetic energy (Fig. 17) or apparent crater volume (Fig. 20) shows that the nuclear explosive is about three times more effective in the 20N12 configuration than in the 20N12P50. Consequently, it would require a nuclear source energy of roughly 60 tons in the 50-cm unstemmed hole to produce the same crater as a 20-ton nuclear source in a stemmed hole

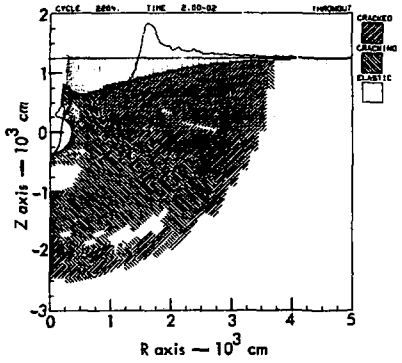

Fig. 34. TENSOR-PUFL ballistic calculation for 20N12P50 at 20 ms.

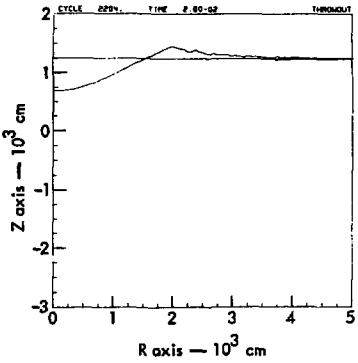

Fig. 35. Apparent crater at 20 ms.

under these particular conditions. The mound kinetic energy and crater dimensions are significantly reduced by the presence of the air stemming rather than Bearpaw shale stemming in the 50-cm hole.

Relationship of Calculations to Cratering Experience in Bearpaw Shale

Some cratering data from experiments in Bearpaw shale are contrasted with the results of our calculations in Fig. 36. In this figure, the scaled, apparent, crater radius, $R_A/(W)^{1/3.4}$, is plotted versus the scaled depth of burst, $DOB/(W)^{1/3.4}$, where R_A is the apparent crater radius in meters, DOB is the depth of burst in meters, and W is the explosive yield in kilotons.* The values used in constructing this figure are summarized in Table 3. Symbols used in the left hand column of Table 3 correspond to those used in Fig. 36.

Figure 36 includes nitromethane experience from 20- and 0.5-ton shots from the series Pre-Gondola I and 1-ton shots from the series Pre-Gondola II - Phase I.[20] There appears to be significantly more scatter in the data for the lower yield (0.5 and 1 ton) nitromethane cratering shots. Effects caused by geological variations from site to site are probably more pronounced for those shallow shots emplaced in or near the weathered surface layers. Other experimental points are from the Diamond Ore Phase IIA cratering experiments with an aluminized ammonium nitrate slurry with yields in the 10- to

*This $W^{1/3.4}$ or $W^{0.3}$ scaling was proposed by Chabai[21,22] and dimensionally represents a compromise between $W^{1/3}$ scaling, which properly scales stresses, and $W^{1/4}$ scaling, which properly scales gravitational effects. The scaling has been applied to a large spectrum of cratering yields, media, and emplacement depths,[20,28] and has been given a more rigorous theoretical treatment by Westine.[24,25]

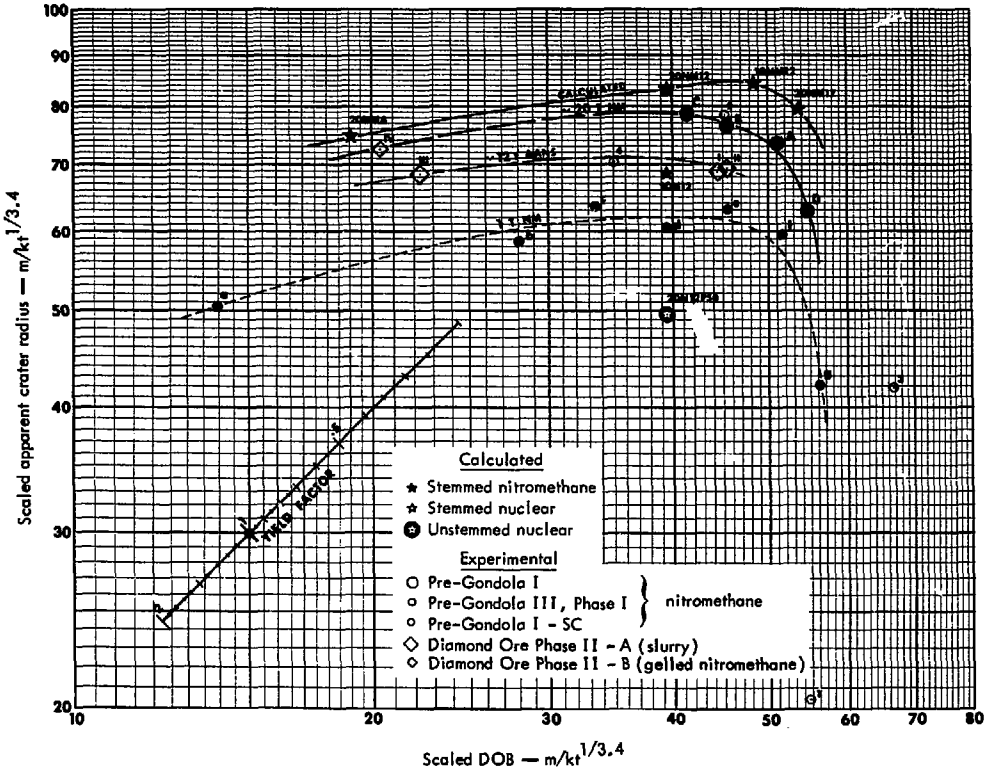

Fig. 36. Apparent crater radius cratering curves for BPS.

Table 3. Cratering data for Bearpaw shale.

	Experiment	Weight, tons	Energy, tons	Depth of burst (DOB), m	Apparent crater radius (R_A), m	Apparent crater depth (D_A), m	Scaled DOB $\left(DOB/W^{1/3.4}\right)$, $m/(kt)^{1/3.4}$	Scaled R_A $\left(R_A/W^{1/3.4}\right)$, $m/(kt)^{1/3.4}$	Scaled D_A $\left(D_A/W^{1/3.4}\right)$, $m/(kt)^{1/3.4}$
	Pre-Gondola I (1966)								
C	Charlie	19.62	19.25	12.95	24.5	9.94	41.4	78.3	31.8
B	Bravo	19.36	18.99	14.10	23.9	8.99	45.2	76.8	28.9
A	Alfa	20.35	19.96	16.07	23.2	9.79	50.8	73.4	30.9
D	Delta	20.24	19.86	17.34	19.8	7.68	54.9	62.9	24.3
4	SC-4	0.5	0.49	3.72	7.47	3.08	35.0	70.2	37.3
2	SC-2	0.5	0.49	4.82	8.32	3.81	45.3	78.3	35.8
1	SC-1[a]	0.5	0.49	5.82	2.16	0.85	54.8	20.4	8.0
3	SC-3[a]	0.5	0.49	7.10	4.45	1.04	66.8	41.9	9.8
	Pre-Gondola III Phase I (1968)								
a	A	1	0.98	1.32	6.55	4.51	14.0	50.3	26.9
b	B	1	0.98	3.66	7.52	3.96	28.1	58.5	30.4
c	C	1	0.98	4.36	8.25	4.26	33.4	63.6	32.7
d	D	1	0.98	5.12	7.86	3.66	39.2	60.3	28.1
e	E	1	0.98	5.94	8.23	3.36	45.6	63.1	27.4
f	F	1	0.98	6.70	7.74	3.27	51.4	59.4	25.7
g	G	1	0.98	7.42	5.45	1.95	56.1	42.1	15.0
h	H	1	0.98	7.99	0.0	0.0	60.8	0.0	0.0
	Diamond Ore Phase II-A (1971)								
I	DOHA-1 (unstemmed)		13.4 ± 1.3	12.5	19.4	7.47	44.4	68.8	26.6
II	DOHA-2 (stemmed)		12.5 ± 1.2	12.5	17.1	6.85	45.4	69.4	25.0
III	DOHA-3 (stemmed)		11.6 ± 1.6	6.0	18.4	6.51	22.3	68.2	45.3
	Diamond Ore Phase II-B (1972)								
IV	DOHB-6M (unstemmed)[c]	17.2	16.9	6.1[b]	21.8	10.2	20.2	72.4	34.0
	Calculated values for stemmed shots:								
	20N12		20	12.5	21.7 (at 30 ms)	9.91	39.5	68.6	31.3
	20NM12		20	12.5	26.3 (at 30 ms)	12.0	39.5	83.1	37.9
	10NM12		10	12.5	*21.7 (at 30 ms)*	9.45	*68.4*	84.1	36.6
	20NM6		20	6.0	23.7 (at 24 ms)	9.08	19.0	74.9	28.7
	20N12P50		20	12.5	15.7 (at 20 ms)	5.61	39.5	49.6	17.7
	20NM17		20	17.0	25.3 (at 40 ms)	11.4	53.7	79.9	36.0

For nitromethane

1 ton(weight) = 0.981 tons (energy)

[a] Anomalous and very asymmetrical; may have produced a mound on level ground.

[b] To center of booster 6.1 m.
To center of charge 6.3 m.

[c] *Private communications from John Diehm and Dave Wooster, Lawrence Livermore Laboratory, (January 1973).*

15-ton range. One nitromethane cratering experiment is included from Diamond Ore Phase IIB. Also shown in the figure are the EJECT results from the TENSOR calculations discussed in the two previous sections.

The measurements of pressure and detonation velocity in the slurry used for Diamond Ore Phase IIA (October 1971) raised serious questions about the reproducibility of the detonation characteristics of this explosive in the field.[1,2,6] The results indicated that DOIIA-1, the unstemmed 12.5-m shot, had a peak pressure and detonation velocity close to the preshot prediction. However, the measured detonation velocities were low on DOIIA-2, the stemmed 12.5-m shot, and DOIIA-3, the stemmed 6-m shot. It appeared as if three different exposives had been used.

In Fig. 36 the cratering points are plotted on a log-log scale. Using the yield factor scale at a 45 deg angle, it is easy to test various possible yield values and make comparisons with the other scaled experimental points. For DOIIA-1, a yield of about 10 tons (instead of 13.4 tons) would raise the point up with the 20-ton NM points. This suggests that about 25% of the slurry energy did not contribute to the cratering process (i.e., went up the air-stemmed hole and/or was not released from the slurry). For DOIIA-2 a yield of about 10 tons (instead of 12.5 tons) would raise the point up with the 20-ton NM points. Since DOIIA-2 was a stemmed shot, this suggests that 20% of the slurry energy was not released for the cratering process. On this shot the measured detonation velocities were lower than predicted. Unfortunately, there are no 20-ton NM stemmed experimental points near the DOIIA-3 value. However, one might assume that the unstemmed DOIIB-6M shot represents a lower bound for the stemmed case. A yield of about 9 tons (instead of 11.6 tons) would raise the points DOIIA-3 close to a line defined by the stemmed Charlie shot and the unstemmed DOIIB-6M shot. This would suggest that about 25% of the slurry energy was not released for the cratering process for DOIIA-3. Detonation velocities measured on DOIIA-3 were also lower than predicted. The above conjectures about the slurry neglect differences that might have been associated with variations in the local site geology.

Figure 37 shows a comparison of experiment and calculated values for scaled apparent crater depth plotted vs scaled depth of burst. Near the "optimum" depth of burst (20NM12), the calculated values generally showed a larger scaled depth than the experimental values. However, near the "half-optimum" depth of burst (20NM6), the experimental values showed a larger scaled depth than the calculated values.

We have not considered the effects of layered geology, except in some of the one-dimensional studies of Ref. 3. This was done with the intent of keeping the results relatively general by not constraining them to a particular experimental site. If one were to conduct a detailed postmortem of a particular event, this omission would not be justified.

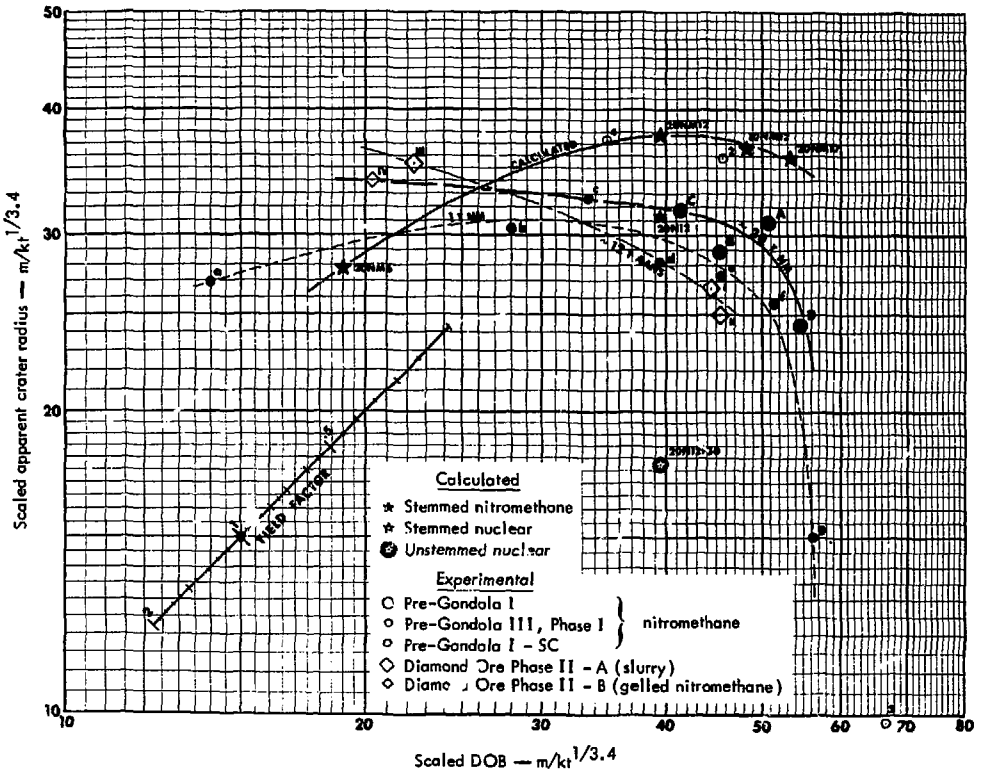

Fig. 37. Apparent crater depth cratering curves for BPS.

Conclusions

Both one-[3] and two-dimensional Lagrangian computer calculations have been performed on Bearpaw shale to model cratering experiments conducted near Ft. Peck, Montana. A close agreement between calculation (the 20-ton nitromethane shot) and experiment (Pre-Gondola I Charlie) was demonstrated. This validated the constitutive parameters used to describe the Bearpaw shale[3] and exhibited the capability of our computational tools. Using results from additional calculations of 20-ton nitromethane shots buried near half and three-halves "optimum" depth (5 and 17 m), computed "cratering curves" for apparent crater radius and depth have been constructed for Bearpaw shale. These theoretical curves were found to be in good agreement with empirical curves for this material.

During this study, a calculational requirement was discovered. For the yields, media, and emplacement configurations addressed in this study, it was necessary to run each computer calculation to at least 20 ms in problem time in order to get the proper final crater shape and constant mound behavior from the ballistic EJECT code.

It was found that a 20-ton nitromethane source was significantly more efficient in coupling energy into the media than a hypothetical 20-ton nuclear source. Based upon our calculations we concluded that cratering phenomena produced by a 20-ton nuclear source buried at "optimum" depth (12.5 m in this medium) were best modeled with a nitromethane source having a yield of about 10 tons of energy. Graphical comparisons of the two cratering sources are shown in the appendices.

The coupled TENSOR-PUFL codes were modified and utilized for the unstemmed cratering configuration with a hypothetical nuclear source. Calculations of an unstemmed configuration having a 50-cm radius emplacement hole showed that a significant amount of source energy was diverted from the cratering process and significantly smaller crater dimensions resulted.

These calculations and new two-dimensional graphical capabilities have greatly improved our understanding of cratering phenomena in Bearpaw shale particularly since they were supplemented by extensive experimental data. They have served as a basis for designing similar experiments and calculations. The experience gained in treating these cratering problems has been quite valuable in simulating cratering experiments in other media in Projects Diamond Ore and Essex.

Acknowledgments

The authors also wish to acknowledge the assistance of Frances Peterson and Eleanor Reed in performing the one-dimensional calculations, and the invaluable support of James G. Shaw in using the two-dimensional computer code. Shirley Campbell assisted with the TENSOR-PUFL code modifications. Barbara K.

Crowley, W. J. Hannon, J. S. Kahn, and R. W. Terhune have provided advice and suggestions throughout the clay shale investigation. The Explosive Excavation Research Laboratory of the U.S. Army Engineer Waterways Experiment Station fielded the high-explosive tests and gathered much of the experimental data used in this study.

A special thank you goes to Lydia Burrow who prepared the initial manuscript as well as its many revisions, Diana Taasevigen who prepared our final draft, Howard Lentzner who edited the report, and the Technical Information Department for producing the final report.

References

1. J. M. O'Connor, T. J. Donlan, and D. E. Burton, Explosive Selection and Fallout Simulation Experiments: Nuclear Cratering Device Simulation (Project Diamond Ore), U.S. Army Engineer Waterways Experiment Station Explosive Excavation Research Laboratory, Livermore, California, Technical Report E-73-6 (1973).
2. C. J. Sisemore, D. E. Burton, and J. B. Bryan, Project Diamond Ore, Phase IIA: Close-In Measurements Program, Lawrence Livermore Laboratory, Rept. UCRL-51620 (1974).
3. B. K. Crowley, D. E. Burton, and J. B. Bryan, Bearpaw Shale: Material Properties Derived from Experiment and One-Dimensional Studies, Lawrence Livermore Laboratory, Rept. UCID-15915 (1971).
4. D. E. Burton, C. M. Snell, and J. B. Bryan, Computer Design of High-Explosive Experiments to Simulate Subsurface Nuclear Detonations, Lawrence Livermore Laboratory, Rept. UCRL-75190 (1973). Accepted for publication in Nuclear Technology.
5. M. Finger et al, Explosive Investigation in Support of Project Diamond Ore, Lawrence Livermore Laboratory (in preparation).
6. F. Helm, R. Boat, M. Finger, and D. Wooster, The Development and Manufacture of a Gelled Nitromethane Explosive for Project ESSEX, Lawrence Livermore Laboratory, Rept. UCRL-51536 (in publication).
7. D. E. Burton and E. J. Leahy, Simulation of Subsurface Nuclear Explosions with Chemical Explosives, U.S. Army Engineer Waterways Experiment Station Explosive Excavation Research Office, Livermore, California, Rept. EERO-TM-71-29, March 1972.
8. J. T. Cherry, S. Sack, G. Maenchen, and V. J. Kransky, Two-Dimensional Stress-Induced Adiabatic Flow, Lawrence Livermore Laboratory, Rept. UCRL-50987 (1970).
9. R. W. Terhune, T. F. Stubbs, and J. T. Cherry, "Nuclear Cratering on a Digital Computer," in Proceedings of Symposium on Engineering with Nuclear Explosives, Las Vegas, 1970 (American Nuclear Society) vol. 1, pp. 334-359 (1970).

10. D. E. Burton and C. M. Snell, User's Guide to: TENPLT (TENSOR Graphics Code) and EOSLIB and XMUPGENS (Auxiliary Data Codes), U.S. Army Engineer Waterways Experiment Station Explosive Excavation Research Laboratory, Livermore, California, Miscellaneous Paper E-74-1 (1974).

11. T. R. Butkovich, The Gas Equation of State of Natural Materials, Lawrence Livermore Laboratory, Rept. UCRL-14729 (1967).

12. L. E. Lee, H. C. Hornig, and J. W. Kury, Adiabatic Expansion of High Explosive Detonation Products, Lawrence Livermore Laboratory, Rept. UCRL-50422 (1968).

13. A. E. Abey, B. P. Bonner, H. C. Heard, and R. N. Schock, Mechanical Properties of a Shale from Site U-2, Lawrence Livermore Laboratory, Rept. UCID-16023 (1972)

14. R. Gates, formerly of the U.S. Army Engineer Waterways Experiment Station Explosive Excavation Research Laboratory, Livermore, California, private communication.

15. T. R. Butkovich, Lawrence Livermore Laboratory, private communication (Memo: UOPKA, Rev. 1, December 1966, Comparison with SOC Code Calculations of Nuclear and High Explosive Detonations in the Same Media).

16. T. R. Butkovich, J. Geophys. Res. 76, 1993 (1971).

17. M. K. Kurtz, et al, "Project Pre-Gondola I, Technical Director's Summary Report," U.S. Army Engineer Nuclear Cratering Group, Livermore, California, Rept. PNE-1102, January 1968.

18. B. K. Crowley and L. K. Barr, TENSOR-PUFL: Boundary Condition Linked Code, Lawrence Livermore Laboratory, Rept. UCRL-72120 (1960) also J. Comp. Phys. 7 (1), 167, 1971.

19. L. K. Barr, Description of the TENSOR-PUFL Fortran Program, Lawrence Livermore Laboratory, Rept. UCRL-50801 (1970).

20. S. M. Johnson, "Explosive Excavation Technology," U.S. Army Engineer Nuclear Cratering Group, Livermore, California, Rept. NCG TR-21, June 1971.

21. J. Chabai, Crater Scaling Laws for Desert Alluvium, Sandia Laboratories, Albuquerque, New Mexico, Rept. SC-4391 (RR) (1959).

22. J. Chabai, J. Geophys. Res. 70, 5075 (1965).

23. E. Teller, W. K. Talley, G. H. Higgins, and G. W. Johnson, The Constructive Use of Nuclear Explosives (McGraw-Hill, New York, 1968) p. 147.

24. W. E. Baker, P. S. Westine, and F. F. Dodge, Similarity Methods in Engineering Dynamics: Theory and Practice of Scale Modeling (Hayden, Rochelle Park, New Jersey (1973) pp. 252-262.

25. P. S. Westine, J. Terramechanics 7, 9 (1970).

Appendices

INTRODUCTION

A cratering equivalence, based on two-dimensional calculations, has been established for 20-ton nuclear and 10-ton nitromethane energy sources buried at a depth of 12.5 m in Bearpaw shale. The comparisons made in the main text between the 20N12 and 10NM12 calculations were generally confined to parameters such as mound mass and crater radii. The primary purpose of the following appendices is to provide more detailed and dynamic comparisons of these two calculations which are referred to here as NUC3 (20N12) and NMTEN (10NM12). More explicitly:

Appendix A compares the contour lines of constant speed at six different times between 2 and 40 ms.

Appendix B compares the isobars (lines of constant pressure) at eight times between 2 and 40 ms.

Appendix C compares the calculated mound and ejecta profiles (ballistic calculations) for six link times between 2 and 40 ms.

Appendix D compares several additional crater parameters at a time of 30 ms. These include: apparent crater profiles, surface velocities, ejecta distributions, tabulated crater parameters, and the brittle fracture parameter (SV1).

Appendix E is directed toward presenting a few of the other graphics options available from the graphics code.

Most of the figures used in this report were generated by a TENSOR graphics and editing code, TENPLT, which was written in conjunction with this work.[10] The EJECT code is currently a subroutine of TENPLT. These figures have been published exactly as created by TENPLT, aside from minor editorial modifications and additions. In each of the figures, the single line above the figure is plotting instructions given TENPLT (e.g. CONTOUR SP LINES).

Many additional graphical results were produced by the computer but they are too voluminous to publish. People interested in them should contact the authors.

APPENDIX A: COMPARISON OF ISO-SPEED (MAGNITUDE OF PARTICLE VELOCITY) CONTOUR LINES FOR 20N12 (NUC3) AND 10NM12 (NMTEN) AT SIX TIMES

In the figures, the cavity boundary is indicated by an arrow. The units are cm and cm/s. The letters a-g have been added to explicity mark some of the contours. The letter "a" corresponds to the last entry in the right-hand margin (10 cm/s); the letter "b", to the next to the last entry (31.63 cm/s); and so forth. In all figures the nuclear calculation is presented at the left of the page; the nitromethane, at the right. In the radial direction (R-AXIS) the grid is shown between 0 and 5000 cm. In the vertical direction (Z-AXIS) the grid is shown between -3000 cm and +2000 cm with the source at the origin and the free surface orginally at +1250 cm. This is the grid size used for most figures in the Appendices.

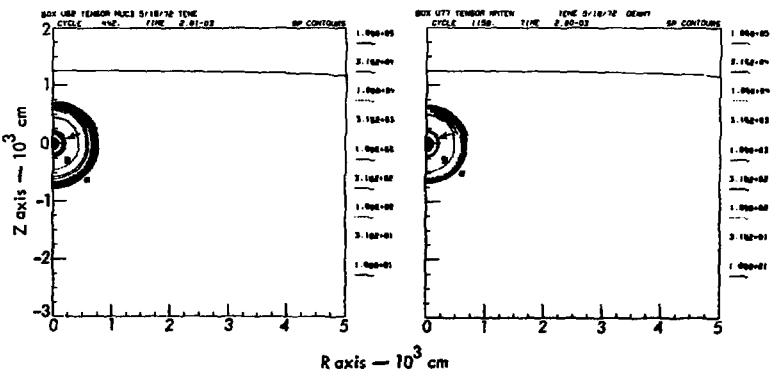

Fig. A1. Comparison of iso-speed contour lines for 20N12 and 10NM12 at 2 ms. The shock wave induced by the nuclear source leads the nitromethane wave because the nuclear cavity pressure is initially higher (~10 Mbar vs ~0.1 Mbar). Thus, the shock velocities are high for the nuclear case in the region close to the source because this material has been shocked to higher stresses.

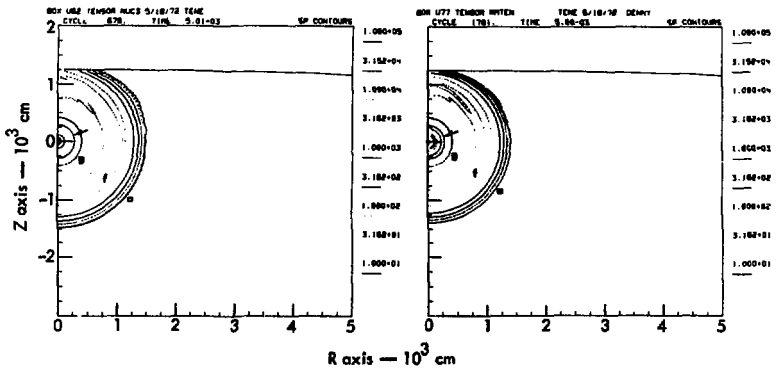

Fig. A2. Comparison of iso-speed contour lines for 20N12 and 10NM12 at 5 ms. The shock wave has intersected the surface, giving rise to the rarefaction which causes turbulence near the surface.

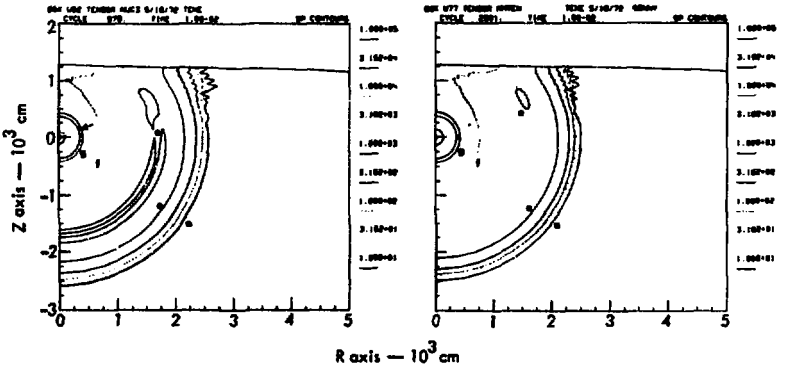

Fig. A3. Comparison of iso-speed contour lines for 20N12 and 10NM12 at 10 ms. The rarefaction has caused an acceleration of some of the material near the surface as indicated by the "f" (3162 cm/s) contour.

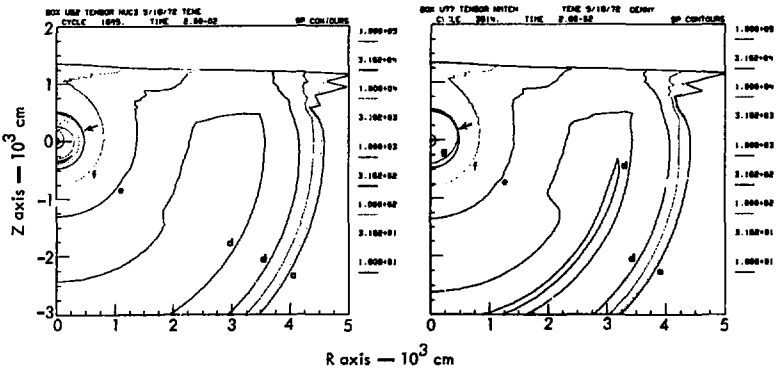

Fig. A4. Comparison of iso-speed contour lines for 20NM12 and 10NM12 at 20 ms. The rarefaction has begun to affect the "d" (316 cm/s) and "e" (1000 cm/s) contours.

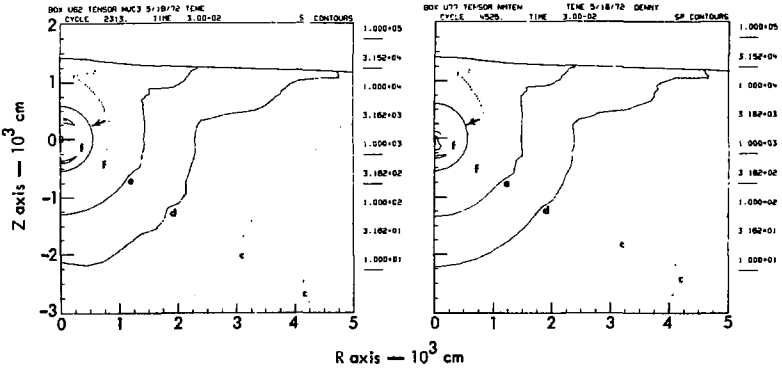

Fig. A5. Comparison of iso-speed contour lines for 20N12 and 10NM12 at 30 ms. The speed fields are very nearly identical. The effects of the rarefaction are clearly visible. At this time the velocity field within the region that will become the mound is well established and will not change significantly at later times.

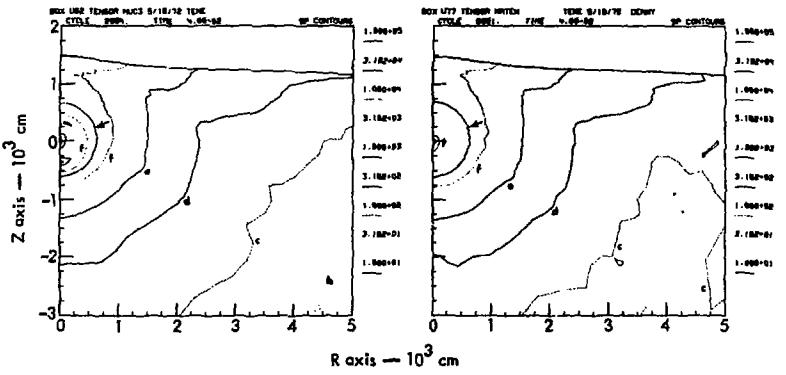

Fig. A6. Comparison of iso-speed contour lines for 20N12 and 10NM12 at 40 ms. Within the mound region the speed fields are quite similar. The nitromethane cavity is slightly larger than the nuclear cavity at this time. The cavities are slightly asymmetrical due to the preferential growth toward the free surface.

APPENDIX B: COMPARISON OF ISOBARS FOR 20N12 (NUC3) AND 10NM12 (NMTEN) AT EIGHT TIMES

The contour lines are labelled in the same manner as those of Appendix A. The units are cm and dyne/cm^2, so that the "a" contour lines correspond to a pressure of 10^7 dynes/cm^2 or 10 bars.

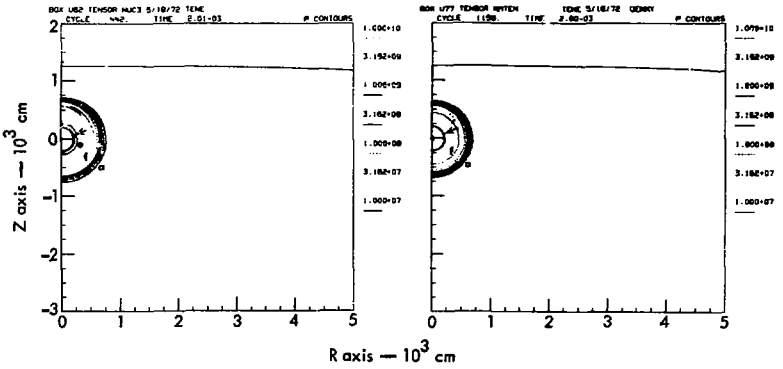

Fig. B1. Comparison of isobars and 20N12 and 10NM12 at 2 ms. The nuclear shock front is leading the nitromethane front because of the initially higher nuclear cavity pressure. By this time the nuclear cavity pressure is below that of the nitromethane.

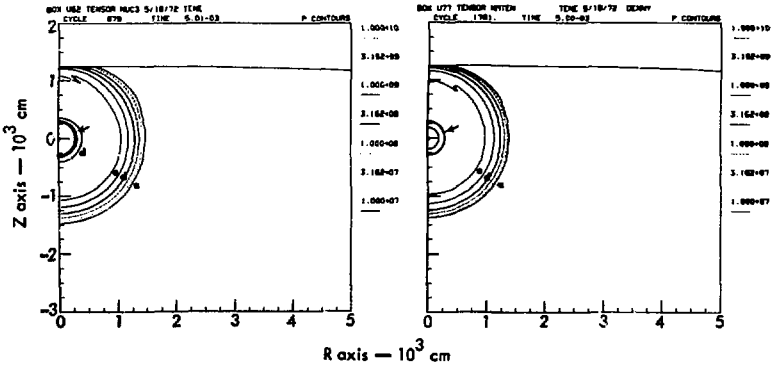

Fig. B2. Comparison of isobars for 20N12 and 10NM12 at 5 ms. The shock fronts are intersecting the preshot ground surface and the rarefaction is beginning to form. No "d" contour (316 bar) appears immediately outside the nitromethane cavity, indicating higher pressure in the HE cavity.

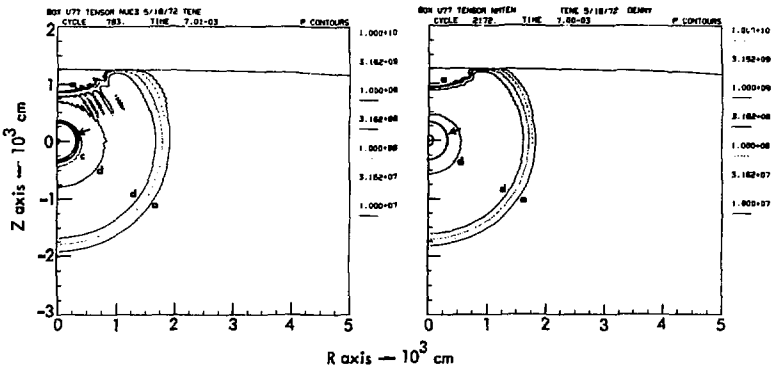

Fig. B3. Comparison of isobars for 20N12 and 10NM12 at 7 ms. The rarefaction has caused material near the surface to spall off, thereby relieving the stresses in this region. The appearance of the "a" contour (10 bar) near the surface is evidence of this. The "rills" which appear in the nuclear problem below the rarefaction are not apparent in the HE problem for this particular choice of contour interval.

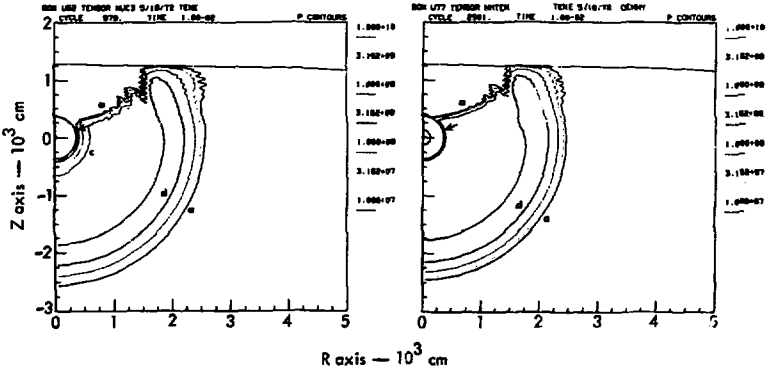

Fig. B4. Comparison of isobars for 20N12 and 10NM12 at 10 ms. The pressure fields appear to be identical except in the vicinity of the cavity where the effects of the lower gas pressure in the nuclear cavity result in contour lines which circle beneath the cavity.

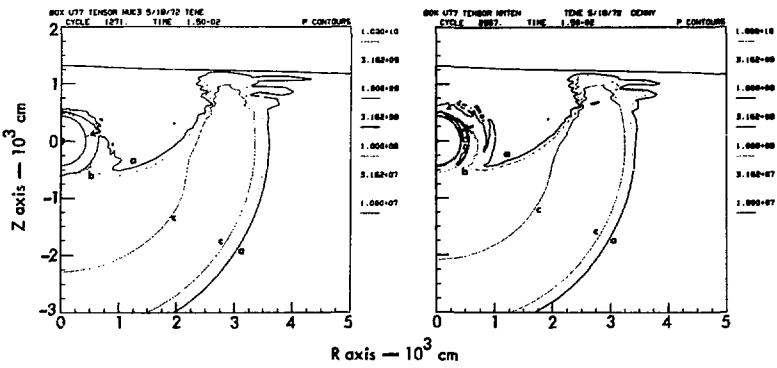

Fig. B5. Comparison of isobars for 20N12 and 10NM12 at 15 ms. The pressure fields are similar except near the cavity. The HE shock front appears to be somewhat broader as indicated by the "c" (100 bar) contours. The effects of the rarefaction are apparent in the "a" contour (10 bar).

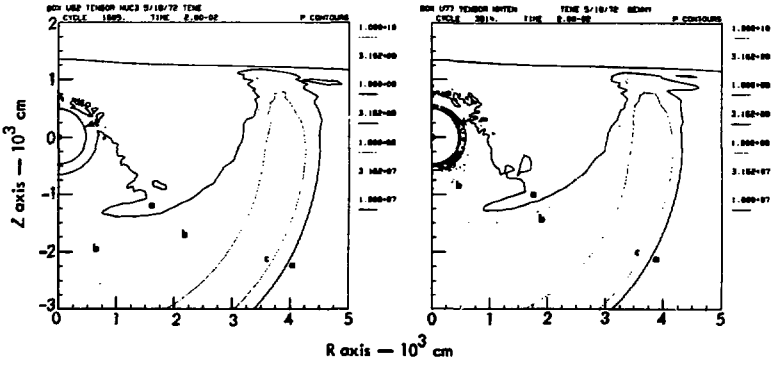

Fig. B6. Comparison of isobars for 20N12 and 10NM12 at 20 ms. By this time, the pressure in the region that will become the mound is well below 10 bar except near the sources. The location of the "b" (31.6 bar) contours is indicative of the difference in source pressures.

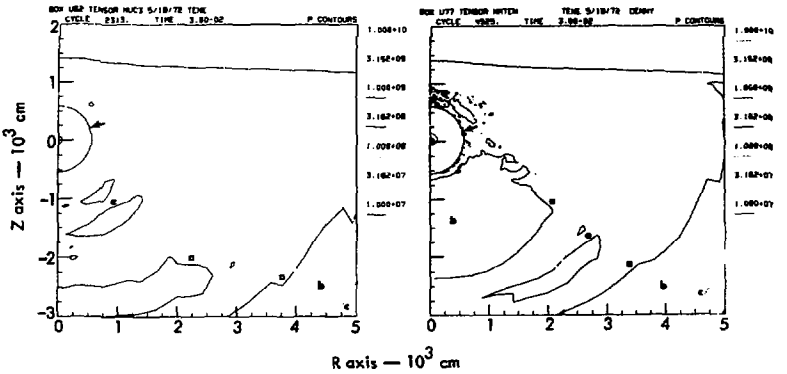

Fig. B7. Comparison of isobars for 20N12 and 10NM12 at 30 ms. The stress fields are beginning to appear to be quite different. The stresses are too low, however, to affect any of the cratering mechanisms. At the right, the rarefaction has caught up with the trailing edge of the shock front.

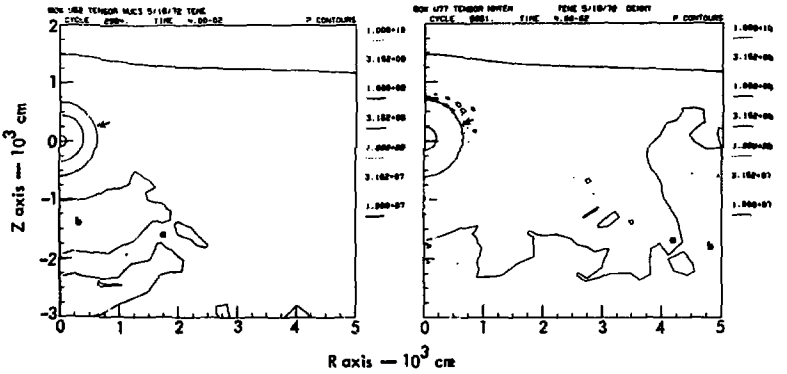

Fig. B8. Comparison of isobars for 20N12 and 10NM12 at 40 ms

APPENDIX C: COMPARISON OF BALLISTIC CALCULATIONS *FOR 20N12 (NUC3) AND 10NM12 (NMTEN) AT SIX LINK TIMES*

At unrealistically early link times (i.e., before about 10 ms) the "mound" appears as a fan-shaped region which moves upward with the shock wave until it intersects the surface after 5 ms. After this time, more physical mound and ejecta profiles are seen. The shaded regions below the mound (after 10 ms) indicate the type of constitutive relation (cracking, cracked, or elastic) being used by TENSOR at that instant (see Cratering Calculations for Stemmed Nitromethane and Nuclear Explosives). After 10 ms, there appears to be little variation in the mound or ejecta profiles aside from that due to cavity growth.

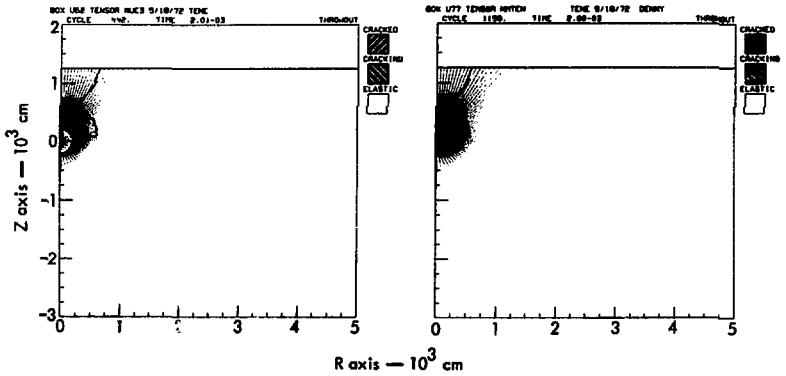

Fig. C1. Comparison of ballistic calculations for 20N12 and 10NM12 at 2 ms.

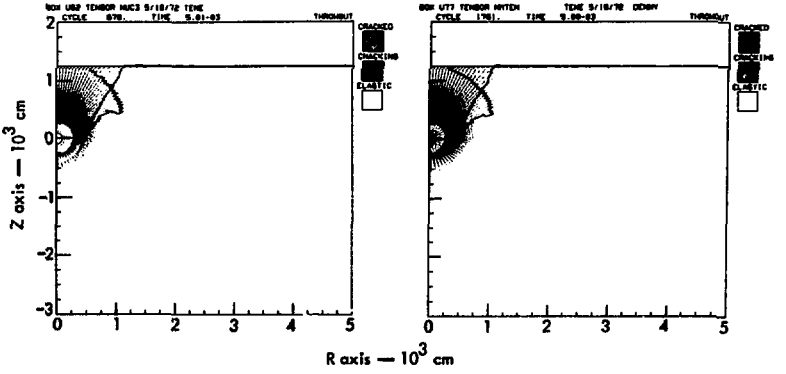

Fig. C2. Comparison of ballistic calculations for 20N12 and 10NM12 at 5 ms.

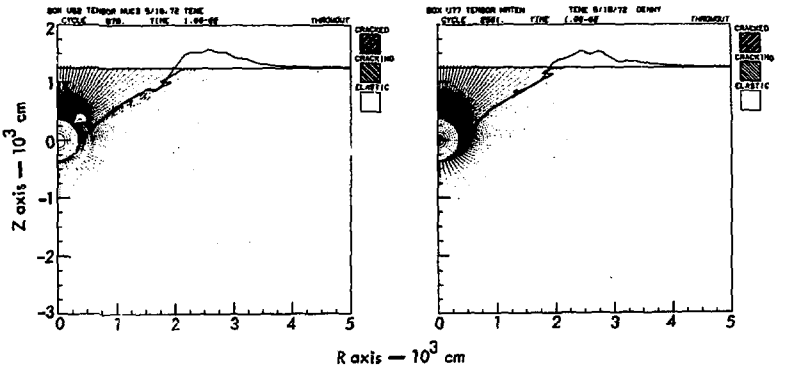

Fig. C3. Comparison of ballistic calculations for *20N12* and *10NM12* at *10* ms.

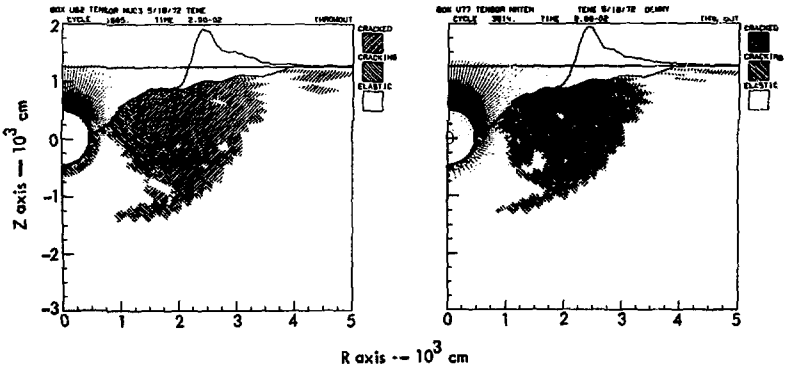

Fig. C4. Comparison of ballistic calculations for 20N12 and 10NM12 at 20 ms.

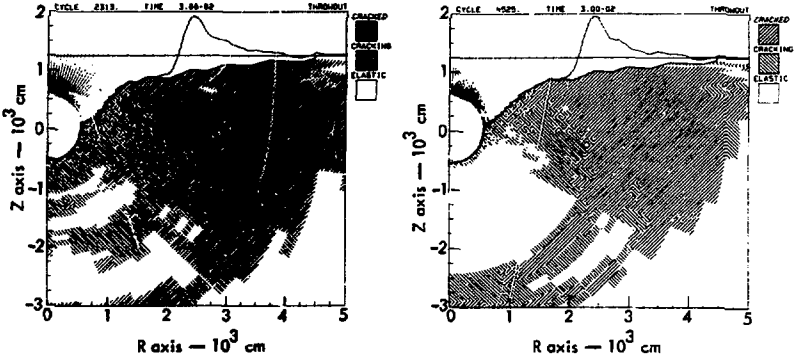

Fig. C5. Comparison of ballistic calculations for 20N12 and 10NM12 at 30 ms.

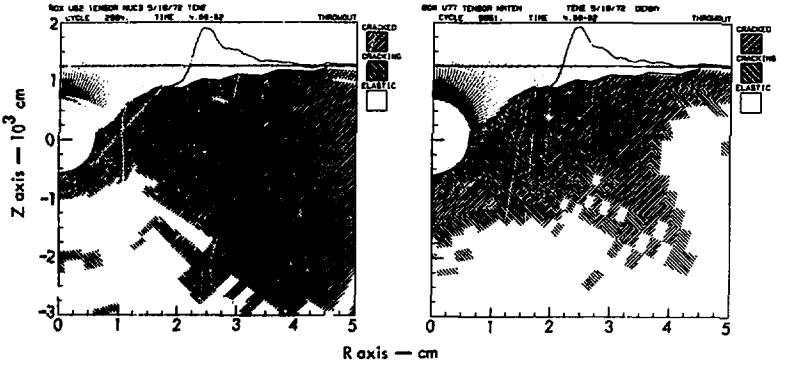

Fig. C6. Comparison of ballistic calculations for 20N12 and 10NM12 at 40 ms.

APPENDIX D: COMPARISON OF 20N12 (NUC3) AND 10NM12 (NMTEN) CRATERING CALCULATIONS AT 30 ms (LINK TIME)

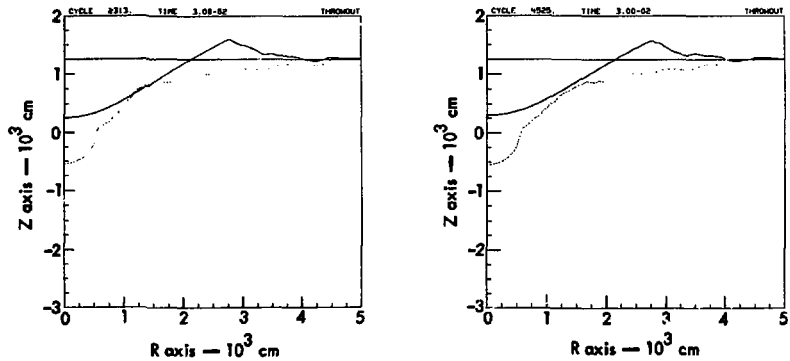

Fig. D1. Comparison of apparent crater profiles for 20N12 and 10NM12 showing the preshot ground surface, mound boundary, and apparent crater profile.

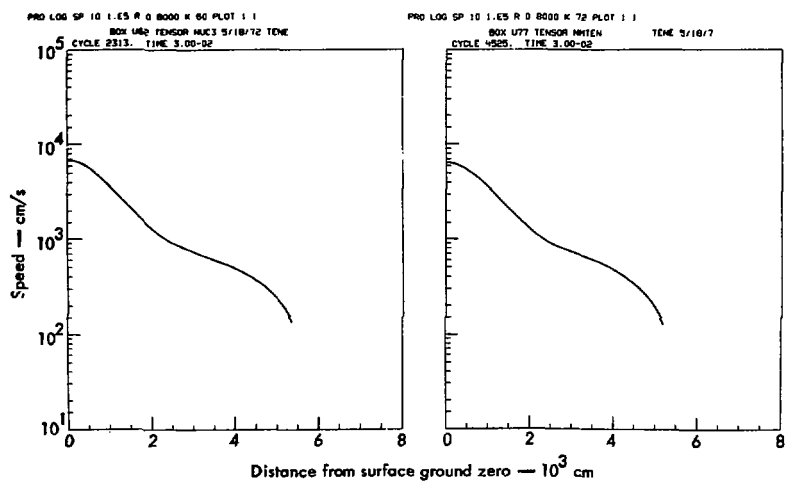

Fig. D2. Comparison of surface velocity profiles for 20N12 and 10NM12. The calculated speed of the ground surface is plotted versus distance from surface ground zero. Units are cm/s. The nuclear problem shows slightly higher surface velocities at this time.

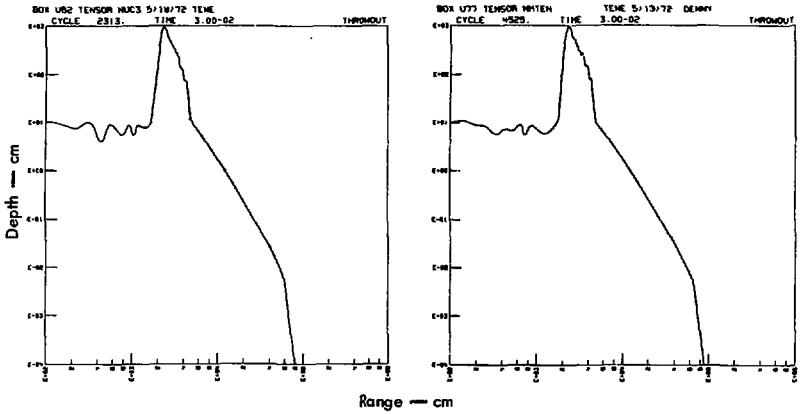

Fig. D3. Comparison of ejecta depths for 20N12 and 10NM12. The calculated ejecta depth (cm) before sloughing is plotted versus range (cm).

BOX U82 TENSOR NUC3 5/18/72 TENE			
TIME	3.001-02		
CYCLE	2313.		
TAPE	NUC0030	DOB	1.250+03
CRITERIA:		MOUND:	
BARRIER	1.250+03	MASS	3.193+10
BULKING FACTOR	1.200+00	INITIAL VOLUME	1.445+10
STABLE SLOPE	3.500+01	MOMENTUM	4.538+13
CONTINUOUS EJECTA	5.000+00	KINETIC ENERGY	6.613+16
DEPTH PARAM	5.000+02	VERTICAL	4.918+16
REBOUND RADIUS	0.	HORIZONTAL	1.695+16
APPARENT CRATER:		EJECTA:	
RADIUS	2.172+03	RADIUS	7.387+03
DEPTH	9.906+02		
VOLUME	6.372+09		
CRATER LIP:		MISSILE RANGE:	
RADIUS	2.778+03	MAXIMUM	6.412+04
HEIGHT	3.454+02	R	4.142+02
VOLUME	1.257+10	Z	4.025+02
TRUE CRATER:			
RADIUS	4.545+03		
DEPTH	1.789+03		
VOLUME	1.610+10		

BOX U77 TENSOR NMTEN TENE 5/18/72 DENNY			
TIME	3.001-02		
CYCLE	4525.		
TAPE	NM10124525	DOB	1.250+03
CRITERIA:		MOUND:	
BARRIER	1.250+03	MASS	3.227+10
BULKING FACTOR	1.200+00	INITIAL VOLUME	1.460+10
STABLE SLOPE	3.500+01	MOMENTUM	4.753+13
CONTINUOUS EJECTA	5.000+00	KINETIC ENERGY	7.344+16
DEPTH PARAM	5.000+02	VERTICAL	5.384+16
REBOUND RADIUS	0.	HORIZONTAL	1.961+16
APPARENT CRATER:		EJECTA:	
RADIUS	2.172+03	RADIUS	7.036+03
DEPTH	9.446+02		
VOLUME	6.084+09		
CRATER LIP:		MISSILE RANGE:	
RADIUS	2.778+03	MAXIMUM	7.868+04
HEIGHT	3.197+02	R	3.681+02
VOLUME	1.183+10	Z	4.637+02
TRUE CRATER:			
RADIUS	4.495+03		
DEPTH	1.804+03		
VOLUME	1.630+10		

Fig. D4. Comparison of tabulated crater parameters for 20N12 and 10NM12. All values are in c.g.s. units.

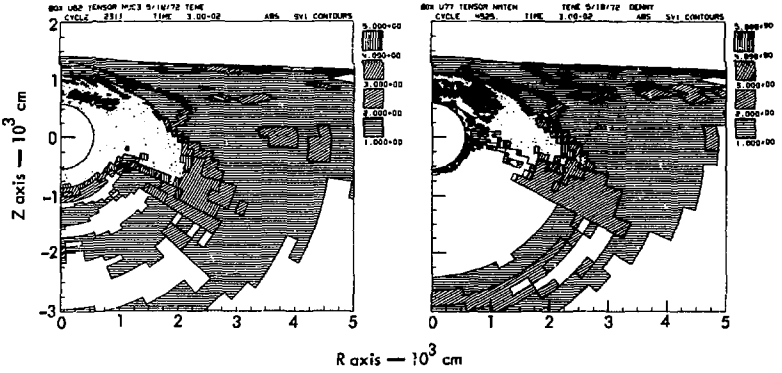

Fig. D5. Comparison of crack parameter (SV1) for 20N12 and 10NM12. The dotted regions correspond to an SV1 value of 5 or greater. SV1 is an indicator of the frequency of brittle failure. Failure associated with plastic deformation is not accounted for by SV1.

APPENDIX E: SOME OTHER AVAILABLE TENPLT OPTIONS

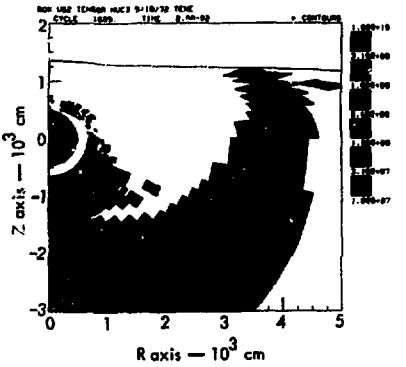

Fig. E1. Pressure contours for 20N12 (SHADE option). Produces more easily identifiable contour regions than the LINES option used in Appendices A and B.

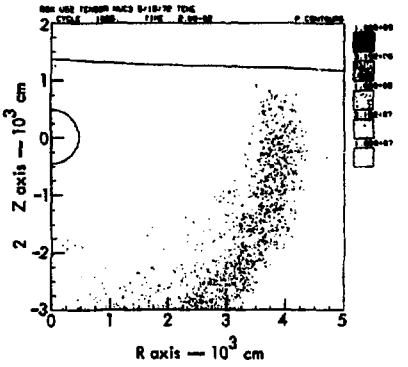

Fig. E2. Pressure contours for 20N12 (DOTS option). Produces somewhat quantitative contour plot in which the density of the random dot pattern is related to the pressure.

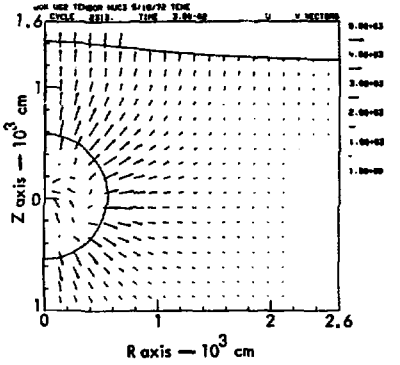

Fig. E3. Velocity vectors for 20N12. Velocity vectors need not coincide with TENSOR nodes.

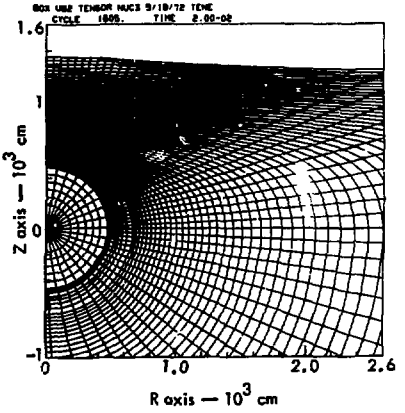

Fig. E4. Zonal boundaries for a portion of the TENSOR grid for 20N12.

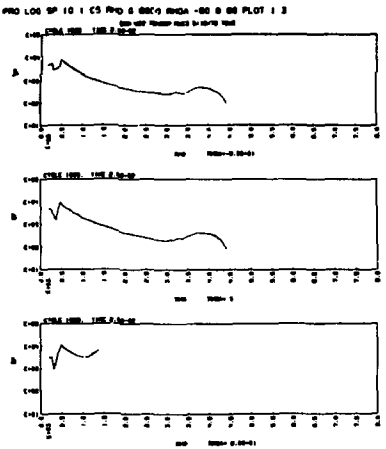

Fig. E5. Semi-log speed profiles for 20N12 for three latitudes. Speed is plotted versus slant range (RHO) in three directions from ground zero. From one to nine plots can be produced per frame. Logarithmic or linear scales can be chosen.

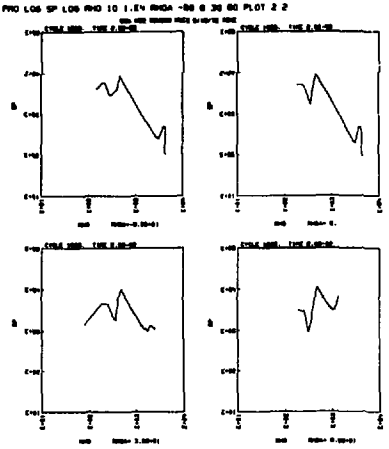

Fig. E6. Log-log speed profiles for 20N12 for four latitudes.

HLL/lc/edas